

# Flux density monitoring of 89 millisecond pulsars with MeerKAT

P. Gitika<sup>1,2</sup>, <sup>\*</sup>M. Bailes<sup>1,2</sup>, R. M. Shannon<sup>1,2</sup>, D. J. Reardon<sup>1,2</sup>, A. D. Cameron<sup>1,2</sup>, M. Shamohammadi<sup>1,2</sup>, M. T. Miles<sup>1,2</sup>, C. M. L. Flynn<sup>1,2</sup>, A. Corongiu<sup>3</sup>, M. Kramer<sup>4</sup>

<sup>1</sup>Centre for Astrophysics and Supercomputing, Swinburne University of Technology, Mail H39, PO Box 218, VIC 3122, Australia.

<sup>2</sup>ARC Centre of Excellence for Gravitational Wave Discovery (OzGrav), Swinburne University of Technology, Mail H11, PO Box 218, VIC 3122.

<sup>3</sup>INAF - Osservatorio Astronomico di Cagliari, Via della Scienza 5, I-09047 Selargius.

<sup>4</sup>MPI für Radioastronomie, Auf dem Hügel 69, 53121 Bonn, Germany.

Accepted XXX. Received YYY; in original form ZZZ

## ABSTRACT

We present a flux density study of 89 millisecond pulsars (MSPs) regularly monitored as part of the MeerKAT Pulsar Timing Array (MPTA) using the L-Band receiver with an approximately two week cadence between 2019–2022. For each pulsar, we have determined the mean flux densities at each epoch in eight  $\sim 97$  MHz sub-bands ranging from 944 to 1625 MHz. From these we have derived their modulation indices, their average and peak-to-median flux densities in each sub-band, as well as their mean spectral indices across the entire frequency range. We find that the vast majority of the MSPs have spectra that are well described by a simple power law, with a mean spectral index of  $-1.86(6)$ . Using the temporal variation of the flux densities we measured the structure functions and determined the refractive scintillation timescale for seven. The structure functions provide strong evidence that the intrinsic radio luminosities of MSPs are stable. As a population, the average modulation index at 20 cm wavelengths peaks near unity at dispersion measures (DMs) of  $\sim 20$  pc cm<sup>-3</sup> and by a DM of 100 pc cm<sup>-3</sup> are closer to 0.2, due to refractive scintillation. We find that timing arrays can improve their observing efficiency by reacting to scintillation maxima, and that 20 cm FRB surveys should prioritise highly scintillating mid-latitude regions of the Galactic sky where they will find  $\sim 30\%$  more events and bursts at greater distances.

**Key words:** flux densities – pulsars – gravitational waves – fast radio bursts – interstellar medium

## 1 INTRODUCTION

Timing millisecond pulsars has a large number of astrophysical applications, including the mass measurements of neutron stars (Thorsett & Chakrabarty 1999) and the pursuit of nanohertz frequency gravitational wave detection using arrays of precisely timed MSPs known as pulsar timing arrays (PTAs) (Detweiler 1979; Hellings & Downs 1983).

PTAs (e.g. Agazie et al. 2023; Zic et al. 2023; Antoniadis et al. 2023) observe the same MSPs over many years, providing extended and comprehensive data sets that can be used for a wide range of investigations including polarimetry and flux density monitoring (Stairs et al. 1999; Kramer et al. 1999; Ord et al. 2004; Dai et al. 2015).

Radio astronomers often use catalogued flux densities, pulse shapes and spectral indices to predict the timing precision they can achieve in a given time with their radio telescope based upon the radiometer equation (e.g. Bailes 2010). The pulsar population’s flux densities and pulse shapes can also be used to estimate the total galactic pulsar population (Levin et al. 2013) and the yields of future surveys with instruments such as the Square Kilometre Array (SKA) (Smits et al. 2009; Keane et al. 2015; Xue et al. 2017).

The majority of radio pulsars have been discovered in large area unbiased surveys and it is common practice to publish their mean ra-

dio flux densities along with their rotational, binary and astrometric parameters (e.g. Manchester et al. 2001; Boyles et al. 2013). Some survey papers use simple calibrations that rely upon the radiometer equation to estimate the flux density of the newly discovered pulsars (Manchester et al. 2001), whilst others usually use more reliable calibration procedures involving a pulsed calibrator signal combined with observations of a reference radio source such as Hydra A (Sobey et al. 2021). Some pulsars that are being routinely observed as part of timing programs provide flux densities that ultimately appear in the pulsar catalogue. Version 1.69 of the ATNF radio pulsar catalog (Manchester et al. 2005) lists flux density estimates for 2344 pulsars at a radio frequency of 1400 MHz. Unfortunately, the mean flux densities of pulsars in the literature often vary. This is partly because many pulsars exhibit variations in their flux densities between observing epochs due to interstellar scintillation, but possibly also because of the methodologies and calibration procedures used.

Radio pulsar flux densities vary for many reasons and on different timescales. Indeed, confirmation of the first pulsar discovered (B1919+21) (Hewish et al. 1968), failed on the first attempt due to unfavourable interstellar scintillation that deamplified the pulsar’s flux density resulting in a non-detection.

Flux density variations can be classified as due to intrinsic or extrinsic reasons.

Here we define intrinsic causes as those which do not depend upon the nature of the bulk of the interstellar medium between the observer and the pulsar along the line of sight. These include magnetospheric

\* E-mail: pgitika@swin.edu.au

changes that lead to both pulse-to-pulse variations, and nulling. Although the mean pulse profiles of pulsars are usually stable, their individual pulses vary in amplitude and shape. These pulse-to-pulse variations are sometimes known as pulse ‘jitter’ (Cordes & Downs 1985; Miles et al. 2022). Some pulsars often switch between two or more distinct mean pulse profiles or radio emission states known as mode changing (Backer 1970b) and in another observed phenomena the radio pulses can cease completely for a few to many tens of rotation periods, a phenomena known as pulse nulling (Backer 1970a). A special class of pulsars known as intermittent pulsars behave as regular pulsars for certain intervals of time and then turn off completely for what can be months (Kramer et al. 2006). In this paper we will only consider the pulsar flux density that is the average of many 100s to 1000s of rotations and thus ignores flux density variations due to pulse jitter. In rare circumstances, precession of a pulsar’s spin axis due to relativistic spin-orbit coupling can change our line of sight through the emission cone and change the flux density of the pulsar. The best known example of this was exhibited by the B pulsar in the double pulsar which completely faded from view and is now invisible (Kramer et al. 2021a). The final form of intrinsic variation arises from eclipses of the pulsar by a companion. This can lead to either severe attenuation or complete non-detection of the pulsar such as in the case of the eclipsing pulsar PSR B1259–63 that orbits a Be star (Johnston et al. 1992).

Radio pulsars also experience changes in their mean flux densities because of the propagation of their radiation through the ionised interstellar medium (IISM) which we consider to be extrinsic in nature. The IISM causes the radio emission to experience refractive and diffractive scintillation that change the phase and path length of the radiation on its way to the Earth. The interference of the radio waves can result in strong flux density variations in both frequency and time, on a timescale between a few seconds to several hours, known as diffractive scintillation. Several studies have been performed to study diffractive scintillation effects, which have been often interpreted successfully using the ‘thin screen scattering’ model (Rickett 1969; Cordes et al. 1986; Armstrong et al. 1995). Using the derived diffractive scintillation parameters of bandwidth and timescale as a function of both day of year and orbital phase, a pulsar’s mean transverse velocity and orientation of the orbit along our line of sight can be estimated (Cordes 1986; Reardon et al. 2020; Askew et al. 2023).

Refractive scintillation is the process of refractive focussing and de-focussing of the pulsar emission due to larger structure electron density fluctuations along our line of sight in the IISM. This causes the flux densities to vary slowly over a long period of time ranging from days to months. The longer timescales involved make studies of refractive scintillation more challenging and involve multi-year campaigns. The long-term variations of pulsar flux densities were first studied by Cole et al. (1970) with the theoretical framework being developed by Scheuer (1968), Rickett et al. (1984) and Cordes et al. (1986). In a 43 consecutive day mean flux density campaign on 25 pulsars with the NRAO 91 m telescope, Stinebring & Condon (1990) demonstrated for the first time that potentially all of the non-nulling “normal” slow pulsars with high dispersion measures had remarkably consistent mean flux densities and that their intrinsic luminosities are probably constant. This was corroborated by a more comprehensive study consisting of daily monitoring over five years of 21 pulsars at a centre frequency of 610 MHz (Stinebring et al. 2000). The pulsars with the highest DMs ( $> 200 \text{ pc cm}^{-3}$ ) showed remarkably low levels of flux modulation of just a few percent. More recently Kumamoto et al. (2021) studied the effects of the IISM by long term monitoring of flux densities of 286 normal pulsars and estimated various scintillation timescales involved. Again they found

that the majority of pulsars with large DMs had low modulation indices, consistent with constant intrinsic radio luminosities. Their only exceptions appeared to be subject to obvious nulling or eclipsing behaviour.

Millisecond pulsars are steep spectrum objects, and at 20 cm wavelengths often have power law spectra with power law indices most often between  $-1$  to  $-3$ . Kramer et al. (1998) monitored 23 MSPs with the 100 m Effelsberg radio telescope and found their mean spectral index was  $-1.8(1)$  whilst Kramer et al. (1999) found the mean spectral index of  $-1.76(14)$  for a wider range of frequencies extending up to  $\sim 4.9$  GHz. Toscano et al. (1998) performed a comprehensive study of pulsar flux densities to explore the spectra of 19 MSPs with the Parkes 64 m radio telescope using three different receivers. They found that the MSPs in their study had spectral indices that ranged between  $-1.1$  for PSR J0437–4715 and  $-2.9$  for PSR J1804–2718 with a mean of  $-1.9(1)$ . Recently Jankowski et al. (2018) explored the flux densities and spectral properties of 441 pulsars. They found that 70% of all the pulsars in their study could have their spectra defined by a simple power law, but others were better modelled with a spectral break, whilst others needed a curved spectrum. In a study of the mean flux densities of 24 MSPs in three frequency bands Dai et al. (2015) showed that most MSPs were also well described by a single power law spectra, with a few exceptions such as PSR J1600–3053 (which shows a flattening of its spectrum below 1 GHz). Most recently Spiewak et al. (2022) measured the spectral indices of 189 MSPs with the MeerKAT radio telescope and found a mean spectral index of  $-1.92(6)$ , very close to other mean values in the literature.

Stable flux density measurements of the high-DM slow pulsars suggests that pulsars have intrinsically stable radio luminosities over long timescales and the observed variations in the flux densities can be attributed to fluctuations in the turbulent plasma in the IISM. This may not be very surprising. Most pulsars are millions of years old and have only been observed for a few tens of years. If they have stable magnetic fields and orientations, they might be expected to be intrinsically stable radio emitters. One way to characterise the changes in flux is to define a refractive scintillation timescale that reflects the timescale over which pulsar fluxes are correlated. Stinebring et al. (2000) and more recently Wang et al. (2023) studied the flux density variations of 21 and 151 pulsars respectively. This enabled them to estimate the refractive scintillation timescales of 21 and 15 pulsars respectively, and Wang et al. (2023) measured the modulation indices of 95 pulsars and 39 of their pulsars had a pulse period less than 20 ms. Although their study only included 14 MSPs with DMs greater than  $100 \text{ pc cm}^{-3}$  they possessed a mean modulation index (standard deviation / mean flux density) of 0.23. This suggests that any intrinsic variations are less than this and therefore, like many of the slow pulsars, MSPs might also have stable intrinsic radio luminosities.

The new 64-antenna MeerKAT telescope located in the Karoo, South Africa provides an opportunity to revisit and monitor the flux densities of MSPs in the southern sky (Bailes et al. 2020). The MeerKAT Pulsar Timing Array (MPTA) is one of four major project themes in the MeerTime project (Spiewak et al. 2022; Miles et al. 2023). The principal goal of the MPTA is to detect nanohertz frequency gravitational waves (GWs).

Long term monitoring of MSP flux densities can contribute to optimising the observation strategy for the faster detection of GWs. If pulsars experience long-term refractive scintillation that leads to predictable fluxes over many months we may choose to dwell longer on them when they are bright, and spend less time observing them when they are faint. Decades of MSP flux density monitoring by the

PTAs will also assist in gaining a better understanding of the IISM if their radio luminosities are intrinsically stable.

In this work, we measured the flux density variability of the 89 MSPs that are part of the MPTA program across nearly an octave of bandwidth with a centre frequency near 1284 MHz over many epochs spanning 3.3 years. In Section 2.1, a brief summary of the pulsar sample and observations is provided before we discuss the data reduction and flux density calibration process in Section 2.2. In Section 3, we present our results, including the mean flux densities, spectral indices, modulation indices, and temporal flux density structure functions. In Section 4, we look at some of the aggregate properties of the pulsar sample and their implications for timing arrays and FRBs discovered at high galactic latitudes (Thornton et al. 2013). Finally, we draw our conclusions in Section 5.

## 2 OBSERVATIONS AND DATA REDUCTION

### 2.1 Pulsar sample

The MeerKAT radio telescope regularly observes 89 MSPs under the MeerTime MPTA project (Miles et al. 2023). These pulsars were distilled from a longer list of 189 timing array pulsar candidates (Spiewak et al. 2022) and chosen for their precision timing potential. They were observed irregularly at first while the source list was being optimised, and then with an approximately 2-week cadence. Almost all of the pulsars have shown great timing precision potential with mostly sub-microsecond residual timing errors many using only 256 s long observations (Miles et al. 2023). However, one pulsar, PSR J1756–2251, has now been removed from the MPTA project as its timing precision is not sufficient for retention in the PTA. This pulsar was, nevertheless, retained in our flux density study.

Our data reduction procedure is identical to that described in Spiewak et al. (2022) and a brief summary is presented here. The observations were carried out using the L-band (856–1712 MHz) receiver of MeerKAT with 1024 frequency channels. The uppermost and lowermost 48 channels of the band were removed to avoid data affected by bandpass roll-off, leaving 775.75 MHz of bandwidth centred at 1284 MHz. All of the observations then have 928 frequency channels which were integrated into 8 sub-bands for the flux density calculations after radio frequency interference (RFI) mitigation algorithms were applied. The observations typically range from 4–30 min except for some very long observations ( $\sim$  several hours) that were obtained as part of the RelBin project (Kramer et al. 2021b) that also observes a subset of the pulsars to study the relativistic effects in binary pulsars. The aim of our experiment was to explore the flux densities of well-separated observations (i.e. separated by a day to several days), so we only considered the flux densities for the first 256 s of each epoch’s observation. This avoids biases in the flux density distributions that can occur if the observations are broken into many (non-time independent) 4 min integrations, and averaging that might occur in long observations. It would be possible in the future to investigate the sub-day temporal scintillation properties of the flux densities using the subset of pulsars that have very long observations (i.e. hours) but this is the topic of other studies aiming to investigate the orbital-phase and day-of-year dependent scintillation properties of some of the relativistic binary pulsars.

Less than 0.5% of the observations failed due to calibration or configuration issues and these were removed prior to our analysis. All the observations use standard templates to help identify RFI-affected observations and were cleaned using the MeerGuard pipeline (Spiewak et al. 2022) before integration of the first 256 s into our final

sample which consists of 8 flux density values per observation. Our data spanned from February 2019 until June 2022. On average, the data comprised of  $\sim$ 70 observations per pulsar with a maximum of 192 observations for PSR J1909–3744, which is often used as a timing calibrator for various timing programs at MeerKAT.

### 2.2 Flux density Calibration

The pulsed cal system at the MeerKAT telescope has non-linearities that make it unsuitable for precise polarimetric and flux density calibration, so we instead used the radiometer equation to estimate the pulsar mean flux densities. The rms noise  $N$  in a radio telescope of gain  $G$  over a bandwidth  $B$  with  $N_p$  orthogonal polarisations in an integration time  $t$  is given by the radiometer equation

$$N = \frac{T_{\text{rec}} + T_{\text{sky}}}{G\sqrt{fBN_p t}} \quad (1)$$

where  $f$  is the effective fraction of the bandwidth due to the shape of the polyphase filters employed in the digital signal processing, and  $T_{\text{rec}}$  and  $T_{\text{sky}}$  are the temperatures of the receiver, and sky respectively. For high precision radiometry, there are additional terms in Eqn 1, such as effects due to spillover. These are typically small and we can safely ignore them in this work. As the emphasis of this paper is on the relative flux densities and how they vary these assumptions are probably reasonable. In a folded pulsar observation of  $N_{\text{bin}}$  phase bins, if there is negligible radio frequency interference, then the pulsar’s mean flux density  $S$  is related to signal-to-noise ratio  $SNR$  in the  $N_{\text{on}}$  on-pulse bins by

$$S = SNR \frac{T_{\text{rec}} + T_{\text{sky}}}{G\sqrt{fBN_p t}} \sqrt{\frac{N_{\text{on}}}{N_{\text{bin}} - N_{\text{on}}}}. \quad (2)$$

The derivation of this equation is given in appendix A. Here SNR should not be confused with the optimal signal-to-noise ratio returned by programs such as `PDMP` from the PSRCHIVE software suite. `PDMP` uses a series of trial pulse widths to find the highest SNR but this neglects the flux in the rest of the on-pulse bins and leads to inaccurate flux densities. The mean flux density can be computed by integrating the counts of the on-pulse bins and subtracting off the best-fit baseline, then determining the average flux density over the entire pulse period. A critical assumption in our analysis was that we could effectively remove the RFI to validate Eqn 2. If so, the MSP flux densities at large DMs should exhibit low levels of variation (i.e. small modulation indices) if they have radio luminosities that are intrinsically stable from epoch to epoch (which as we will see later, appears to be the case). Indeed the temporal structure functions of our pulsar flux densities give us great confidence that our approach to calibration is valid.

Flux densities were computed using Eqn 2. We first computed the signal-to-noise ratio SNR of the counts above our baseline. We then took the sky temperatures from the 408 MHz all-sky catalogue (Haslam et al. 1982) at the position of the pulsar scaled as the frequency  $\nu^{-2.6}$  (Lawson et al. 1987) to get the sky background temperature. To compute the system equivalent flux density  $T_{\text{rec}}/G$  as a function of frequency, we used the polynomial fit from SARAO calibrations presented in Geyer et al. (2021). The effective bandwidth of each channel and integration time of the observation was computed after removing RFI-affected channels and sub-integrations, the loss of SNR due to the polyphase filterbank ( $f = 0.91$ ) (Bailes et al. 2020) and the number of on- and off-bins were derived from our standard

**Table 1.** Measured flux densities of the 89 MSPs in our sample.  $N_{\text{obs}}$  is the number of observations for each pulsar and  $S_{944}$ ,  $m_{944}$ ,  $R_{944}$  are the mean flux density, modulation index and ratio of the maximum to median value of the flux density at a central frequency of 944 MHz respectively. Similarly these quantities are given for the 1429 MHz and 1625 MHz sub-bands of the observing frequency band. Spectral index is calculated here using a simple power law model fit to the mean flux density values across the 8 frequency sub-bands. See the data availability section for the results for all 8 of the sub-bands.

NAME	$N_{\text{obs}}$	DM (pc cm <sup>-3</sup> )	$S_{944}$ (mJy)	$m_{944}$	$R_{944}$	$S_{1429}$ (mJy)	$m_{1429}$	$R_{1429}$	$S_{1625}$ (mJy)	$m_{1625}$	$R_{1625}$	Spectral Index
J0030+0451	67	4.3	2.7(2)	0.7(1)	5.4	1.12(5)	0.39(5)	2.6	0.83(3)	0.34(4)	2.3	-2.1(1)
J0101-6422	39	11.9	0.50(10)	1.2(4)	10.6	0.24(2)	0.5(1)	2.6	0.17(1)	0.5(1)	2.9	-1.7(2)
J0125-2327	76	9.6	4.6(4)	0.8(1)	4.6	3.2(2)	0.7(1)	3.5	2.5(2)	0.61(9)	3.4	-1.2(2)
J0437-4715	109	2.6	265(11)	0.45(5)	2.6	137(4)	0.30(3)	2.0	104(3)	0.27(2)	1.9	-1.76(7)
J0610-2100	73	60.7	1.05(4)	0.35(4)	2.0	0.65(4)	0.59(9)	4.4	0.57(4)	0.7(1)	5.3	-1.1(1)
J0613-0200	71	38.8	4.5(1)	0.28(3)	1.8	2.01(9)	0.38(5)	3.0	1.51(7)	0.41(5)	2.9	-1.97(8)
J0614-3329	88	37.1	1.48(7)	0.43(5)	3.2	0.66(6)	0.8(1)	7.2	0.51(4)	0.8(1)	5.4	-1.9(1)
J0636-3044	56	15.5	2.3(5)	1.6(5)	19.9	1.5(2)	1.2(3)	9.0	1.3(2)	1.0(2)	7.2	-0.9(3)
J0711-6830	76	18.4	6.0(7)	1.0(2)	7.5	3.2(6)	1.6(4)	20.7	2.1(3)	1.3(3)	11.1	-1.6(3)
J0900-3144	76	75.7	5.84(7)	0.098(9)	1.3	3.67(5)	0.11(1)	1.2	2.94(4)	0.12(1)	1.3	-1.25(2)
J0931-1902	59	41.5	1.5(1)	0.7(1)	4.6	0.49(6)	0.9(2)	7.5	0.40(6)	1.1(3)	12.2	-2.4(2)
J0955-6150	103	160.9	2.25(5)	0.24(2)	1.8	0.63(2)	0.32(3)	2.1	0.40(2)	0.42(5)	2.2	-3.13(6)
J1012-4235	82	71.7	0.42(1)	0.28(3)	1.8	0.27(1)	0.34(4)	2.3	0.23(1)	0.42(5)	2.8	-1.12(7)
J1017-7156	89	94.2	2.28(9)	0.37(4)	2.3	1.00(5)	0.43(5)	2.7	0.73(4)	0.46(6)	2.8	-2.06(8)
J1022+1001	71	10.3	6.3(8)	1.1(2)	8.3	4.2(4)	0.9(2)	5.6	3.2(3)	0.8(1)	4.9	-1.6(2)
J1024-0719	73	6.5	3.2(6)	1.5(4)	23.2	1.5(1)	0.7(1)	4.7	1.14(9)	0.7(1)	3.9	-1.9(2)
J1036-8317	82	27.1	0.69(4)	0.49(7)	2.8	0.41(4)	0.8(1)	5.5	0.32(3)	0.8(1)	4.0	-1.3(1)
J1045-4509	77	58.1	5.8(2)	0.26(3)	1.7	2.35(9)	0.33(4)	2.1	1.74(7)	0.37(4)	2.2	-2.19(7)
J1101-6424	86	207.4	0.59(1)	0.17(2)	1.5	0.309(6)	0.18(2)	1.5	0.243(6)	0.24(2)	1.7	-1.63(4)
J1103-5403	78	103.9	1.02(7)	0.57(8)	3.0	0.39(2)	0.54(8)	2.8	0.30(2)	0.61(9)	3.8	-2.3(1)
J1125-5825	77	124.8	1.59(4)	0.24(3)	1.8	0.97(3)	0.23(2)	1.8	0.80(2)	0.22(2)	1.6	-1.27(5)
J1125-6014	88	52.9	2.23(5)	0.22(2)	1.8	1.35(5)	0.37(4)	2.5	1.05(5)	0.42(5)	2.7	-1.30(6)
J1216-6410	77	47.4	2.62(5)	0.18(2)	1.5	1.21(4)	0.26(3)	1.9	0.86(3)	0.26(3)	1.7	-1.99(5)
J1231-1411	49	8.1	0.7(1)	1.0(2)	8.5	0.39(5)	0.9(2)	8.1	0.28(4)	0.9(2)	8.3	-1.7(3)
J1327-0755	59	27.9	0.51(7)	1.0(2)	8.1	0.17(2)	1.1(3)	8.4	0.16(3)	1.7(5)	18.3	-2.5(3)
J1421-4409	74	54.6	2.4(1)	0.40(5)	2.3	1.33(7)	0.43(6)	2.7	0.95(5)	0.48(7)	3.1	-1.64(10)
J1431-5740	75	131.4	0.58(2)	0.25(3)	2.0	0.38(1)	0.26(3)	2.4	0.294(8)	0.24(3)	2.0	-1.28(6)
J1435-6100	84	113.8	0.524(8)	0.13(1)	1.3	0.311(7)	0.20(2)	1.6	0.241(6)	0.23(2)	1.7	-1.35(4)
J1446-4701	74	55.8	0.91(6)	0.52(7)	3.0	0.37(3)	0.7(1)	3.8	0.26(3)	0.9(2)	6.3	-2.1(2)
J1455-3330	73	13.6	2.2(3)	1.3(3)	11.3	0.72(9)	1.1(2)	9.5	0.50(5)	0.9(2)	5.1	-2.8(3)
J1513-2550	37	46.9	1.61(7)	0.28(5)	1.4	0.36(1)	0.25(4)	1.7	0.22(1)	0.33(6)	1.6	-3.65(10)
J1514-4946	44	31.0	0.27(3)	0.7(1)	4.2	0.19(2)	0.8(2)	4.5	0.15(2)	1.1(3)	8.8	-1.0(3)
J1525-5545	79	127.0	0.72(1)	0.13(1)	1.5	0.426(6)	0.13(1)	1.4	0.337(5)	0.13(1)	1.5	-1.40(3)
J1543-5149	75	51.0	3.2(1)	0.36(4)	2.4	0.87(6)	0.57(9)	4.4	0.60(4)	0.63(10)	4.0	-3.1(1)
J1545-4550	84	68.4	1.64(6)	0.35(4)	2.1	1.03(4)	0.38(4)	2.6	0.92(4)	0.44(5)	2.5	-1.08(8)
J1547-5709	73	95.7	0.68(3)	0.36(4)	2.0	0.34(1)	0.32(4)	1.9	0.26(1)	0.36(5)	1.9	-1.76(8)
J1600-3053	73	52.3	3.1(1)	0.28(3)	1.7	2.30(8)	0.29(3)	1.9	1.94(7)	0.32(4)	2.0	-0.88(7)
J1603-7202	77	38.0	7.1(5)	0.64(10)	5.5	2.6(2)	0.8(1)	4.7	1.9(2)	0.9(2)	6.3	-2.4(2)
J1614-2230	76	34.5	2.6(1)	0.36(5)	2.2	1.12(6)	0.46(6)	2.3	0.92(6)	0.56(8)	3.7	-1.9(1)
J1628-3205	13	42.1	1.4(1)	0.4(1)	1.9	0.48(7)	0.6(2)	2.8	0.39(7)	0.7(3)	3.2	-2.5(2)
J1629-6902	79	29.5	2.28(10)	0.38(5)	2.3	0.96(7)	0.63(10)	4.6	0.70(6)	0.7(1)	5.5	-2.1(1)
J1643-1224	76	62.4	9.0(1)	0.11(1)	1.3	3.94(6)	0.13(1)	1.3	2.99(6)	0.18(2)	1.4	-2.00(3)
J1652-4838	75	188.2	1.46(3)	0.16(2)	1.3	0.99(2)	0.17(2)	1.6	0.84(2)	0.21(2)	1.6	-1.01(4)
J1653-2054	61	56.5	1.35(6)	0.38(5)	2.4	0.55(3)	0.38(5)	2.2	0.41(2)	0.40(6)	2.2	-2.17(10)
J1658-5324	50	30.8	1.2(1)	0.6(1)	3.8	0.59(9)	1.0(3)	7.9	0.38(5)	0.9(2)	6.0	-2.1(2)
J1705-1903	60	57.5	1.15(6)	0.39(6)	1.7	0.69(3)	0.36(5)	1.9	0.54(2)	0.35(5)	1.9	-1.40(10)
J1708-3506	61	146.8	3.46(5)	0.11(1)	1.2	1.46(2)	0.10(1)	1.2	1.04(2)	0.18(2)	1.2	-2.16(3)
J1713+0747	74	16.0	9.7(8)	0.7(1)	4.6	6.9(9)	1.1(2)	10.5	5.7(7)	1.0(2)	10.5	-1.0(2)
J1719-1438	76	36.8	1.09(6)	0.48(7)	3.2	0.36(3)	0.7(1)	4.8	0.29(4)	1.3(3)	14.4	-2.6(2)
J1721-2457	48	48.2	2.11(8)	0.25(4)	1.5	1.09(7)	0.43(7)	2.2	0.81(5)	0.40(6)	2.2	-1.67(10)
J1730-2304	73	9.6	8.0(5)	0.48(7)	3.1	3.8(4)	0.9(2)	8.9	2.7(4)	1.2(3)	13.4	-1.9(2)
J1731-1847	14	106.5	1.02(4)	0.14(3)	1.2	0.38(2)	0.23(6)	1.2	0.30(2)	0.26(7)	1.3	-2.3(1)
J1732-5049	87	56.8	4.2(3)	0.61(9)	4.4	2.0(2)	0.9(1)	6.0	1.4(1)	0.9(1)	7.1	-1.9(2)
J1737-0811	79	55.3	2.46(7)	0.25(3)	1.5	1.10(3)	0.26(3)	1.7	0.86(3)	0.35(4)	2.1	-1.99(6)
J1744-1134	75	3.1	6.5(8)	1.1(2)	9.5	3.1(4)	1.0(2)	6.0	2.5(3)	1.0(2)	6.4	-1.5(2)
J1747-4036	75	152.9	3.89(9)	0.19(2)	1.5	1.42(2)	0.15(1)	1.4	0.98(3)	0.25(3)	1.7	-2.50(4)
J1751-2857	74	42.8	0.78(2)	0.23(3)	1.6	0.47(1)	0.27(3)	1.8	0.37(1)	0.31(4)	2.2	-1.37(6)
J1756-2251	95	121.2	1.70(2)	0.13(1)	1.2	1.03(2)	0.19(2)	1.4	0.83(2)	0.21(2)	1.4	-1.30(3)
J1757-5322	93	30.8	3.2(1)	0.33(4)	2.1	1.70(9)	0.49(6)	2.7	1.4(1)	0.8(1)	8.2	-1.64(10)
J1801-1417	73	57.3	3.2(1)	0.34(4)	2.0	1.62(7)	0.38(5)	2.6	1.26(6)	0.41(5)	2.6	-1.70(9)

NAME	$N_{\text{obs}}$	DM ( $\text{pc cm}^{-3}$ )	$S_{944}$ (mJy)	$m_{944}$	$R_{944}$	$S_{1429}$ (mJy)	$m_{1429}$	$R_{1429}$	$S_{1625}$ (mJy)	$m_{1625}$	$R_{1625}$	Spectral Index
J1802–2124	72	149.6	2.06(4)	0.16(2)	1.4	0.75(2)	0.18(2)	1.5	0.53(1)	0.20(2)	1.5	-2.47(4)
J1804–2717	36	24.7	3.7(3)	0.5(1)	2.4	1.8(4)	1.2(4)	11.0	1.3(2)	1.1(3)	7.8	-1.8(3)
J1804–2858	45	232.5	1.38(4)	0.18(2)	1.4	0.94(2)	0.12(1)	1.2	0.66(2)	0.18(2)	1.4	-1.46(5)
J1811–2405	119	60.6	3.11(6)	0.20(2)	1.5	1.44(3)	0.22(2)	1.7	1.10(3)	0.26(2)	1.8	-1.90(4)
J1825–0319	73	119.6	0.364(9)	0.21(2)	1.4	0.206(4)	0.18(2)	1.3	0.162(5)	0.26(3)	1.6	-1.51(5)
J1832–0836	54	28.2	1.8(1)	0.49(8)	3.5	1.0(1)	0.8(2)	6.7	0.69(5)	0.6(1)	3.2	-1.7(2)
J1843–1113	73	60.0	1.17(5)	0.37(5)	2.0	0.55(3)	0.47(7)	2.5	0.47(4)	0.7(1)	5.6	-1.7(1)
J1843–1448	38	114.5	0.99(1)	0.08(1)	1.1	0.515(9)	0.11(1)	1.2	0.406(8)	0.13(2)	1.3	-1.70(3)
J1902–5105	78	36.3	3.29(6)	0.15(2)	1.4	0.96(2)	0.19(2)	1.7	0.64(2)	0.23(2)	1.9	-3.02(4)
J1903–7051	90	19.7	1.9(2)	0.8(1)	5.6	0.9(1)	1.1(2)	8.8	0.75(9)	1.1(2)	10.4	-1.8(2)
J1909–3744	192	10.4	3.6(2)	0.86(10)	7.2	1.9(2)	1.3(2)	18.0	1.6(2)	2.0(4)	46.7	-1.5(2)
J1911–1114	39	31.0	2.6(2)	0.6(1)	3.0	0.92(10)	0.7(2)	3.7	0.68(9)	0.9(2)	5.4	-2.5(2)
J1918–0642	76	26.6	3.5(1)	0.27(3)	2.2	1.79(8)	0.38(5)	2.1	1.22(9)	0.61(9)	4.2	-1.84(9)
J1933–6211	95	11.5	2.1(3)	1.2(2)	12.9	1.0(1)	1.4(3)	18.1	0.8(1)	1.3(3)	12.6	-1.8(3)
J1946–5403	75	23.7	0.58(9)	1.3(3)	12.0	0.30(5)	1.6(4)	20.4	0.27(4)	1.4(3)	13.5	-1.3(3)
J2010–1323	77	22.2	1.32(4)	0.28(3)	2.0	0.67(4)	0.46(6)	3.2	0.56(4)	0.58(8)	3.3	-1.59(9)
J2039–3616	74	24.0	1.1(1)	1.1(2)	11.8	0.50(7)	1.2(3)	12.5	0.40(7)	1.5(4)	14.7	-1.7(3)
J2124–3358	77	4.6	11(1)	1.0(2)	7.1	4.9(3)	0.57(8)	3.5	3.5(2)	0.52(7)	2.7	-2.2(2)
J2129–5721	81	31.8	3.8(5)	1.1(2)	11.3	0.9(1)	1.2(3)	14.5	0.58(10)	1.5(4)	21.9	-3.4(3)
J2145–0750	76	9.0	17(2)	1.2(2)	10.7	5.7(8)	1.2(3)	12.7	4.6(5)	1.0(2)	7.5	-2.2(3)
J2150–0326	70	20.7	0.99(8)	0.7(1)	4.8	0.37(5)	1.1(2)	8.4	0.30(4)	1.1(2)	10.7	-2.3(2)
J2222–0137	74	3.3	2.1(3)	1.0(2)	9.5	1.10(10)	0.7(1)	4.5	0.95(8)	0.7(1)	4.2	-1.6(2)
J2229+2643	66	22.7	1.5(2)	1.3(3)	14.8	1.0(3)	2.0(7)	32.1	0.6(1)	1.5(4)	14.9	-1.3(4)
J2234+0944	69	17.8	2.7(5)	1.6(4)	20.0	1.6(2)	1.1(3)	11.6	1.1(1)	1.1(2)	10.7	-1.8(3)
J2236–5527	49	20.1	0.63(8)	0.9(2)	5.9	0.25(4)	1.2(3)	8.1	0.22(4)	1.2(3)	7.5	-2.0(3)
J2241–5236	84	11.4	4.9(6)	1.1(2)	9.4	1.7(1)	0.61(9)	4.3	1.16(7)	0.54(7)	3.8	-2.8(2)
J2317+1439	68	21.9	1.6(2)	0.8(1)	4.6	0.48(8)	1.3(3)	14.5	0.40(9)	2.0(6)	35.1	-2.8(3)
J2322+2057	55	13.4	0.70(9)	0.9(2)	5.9	0.34(5)	1.1(3)	9.5	0.26(5)	1.3(4)	14.5	-1.9(3)
J2322–2650	71	6.1	0.38(4)	1.0(2)	7.0	0.24(1)	0.50(7)	2.7	0.19(1)	0.50(7)	2.8	-1.3(2)

profiles. Each observation was integrated down to 8 frequency sub-bands, and the flux density determined at each epoch. The results are presented in Table 1.

### 3 RESULTS

In this section, we will first present the derived flux densities of our pulsar sample and then quantify their variability by calculating their modulation indices and temporal structure functions. Figure 1 shows the mean flux densities of four of our pulsars (each of which has a very different DM) as a function of both pulse phase and radio frequency. The four pulsars were chosen to show the different types of scintillation exhibited, ranging from those with no extreme minima (except for those induced by interference) such as J0437–4715, those with just one or two bright scintles present in the band like J1909–3744, pulsars with many bright scintles across the band (J1017–7156) and those with almost continuous intensity across the band like J1747–4036. In Figure 2 we show how the flux densities of the same four pulsars change from epoch to epoch. Histograms of their flux densities at a centre radio frequency of 1429 MHz are shown in Figure 4.

#### 3.1 Flux densities

Table 1 lists pulsar names, number of observations, DMs and mean pulsar flux densities measured at three different frequency bands centered at 944, 1429 and 1625 MHz of the 89 pulsars in our sample. We chose these three bands (of the 8) because the 944 and 1625 MHz sub-bands represent the extrema of our 775.75 MHz frequency band and the 1400 MHz sub-band is the most often cited one in

the literature for ease of comparison with other studies. See data availability statement for the values of these quantities at all 8 of the frequency sub-bands. The large number of observations in the sample for each pulsar (typically greater than 70) make it possible to establish robust modulation indices (see Section 3.3) for each of the pulsars. Another very useful quantity to demonstrate the range of amplification experienced by the pulsars is the ratio of maximum flux density value observed and its median. This is a number rarely quantified in the literature but quite instructive when assessing the likelihood that survey candidates should be re-observed in follow-up observations. At 1429 MHz, this ratio has a mean and median value of  $\sim 5$  and  $\sim 3$  respectively for our MSP sample. The maximum value of this ratio at 1429 MHz in our sample was  $\sim 32$  exhibited by PSR J2229+2643 which has a DM of  $22.73 \text{ pc cm}^{-3}$ .

To check that our method for determining the mean flux densities is accurate, we used the study of Dai et al. (2015) for comparison. Their study used a pulsed cal and observations of Hydra A at the Parkes 64 m radio telescope to calibrate their flux densities. They had 21 sources in common with our sample and the ratio of their flux densities to ours had a mean of 1.19 with a reasonably high standard deviation of 0.2. Unfortunately many of their pulsars were part of timing array observations where the observer has discretion to alter the observing schedule. Observers could choose to abandon observations of pulsars that were in a low-flux state, or repeat observations of MSPs experiencing a scintillation maximum, potentially biasing their sample. The highest DM pulsar that was common between our samples was J1017–7156, which agreed with our flux density to within 1% and has a DM of  $94.22 \text{ pc cm}^{-3}$ . Another flux density study by Wang et al. (2023) studied 28 pulsars in common with ours, and with 15 possessing DMs greater than  $60 \text{ pc cm}^{-3}$ . The average

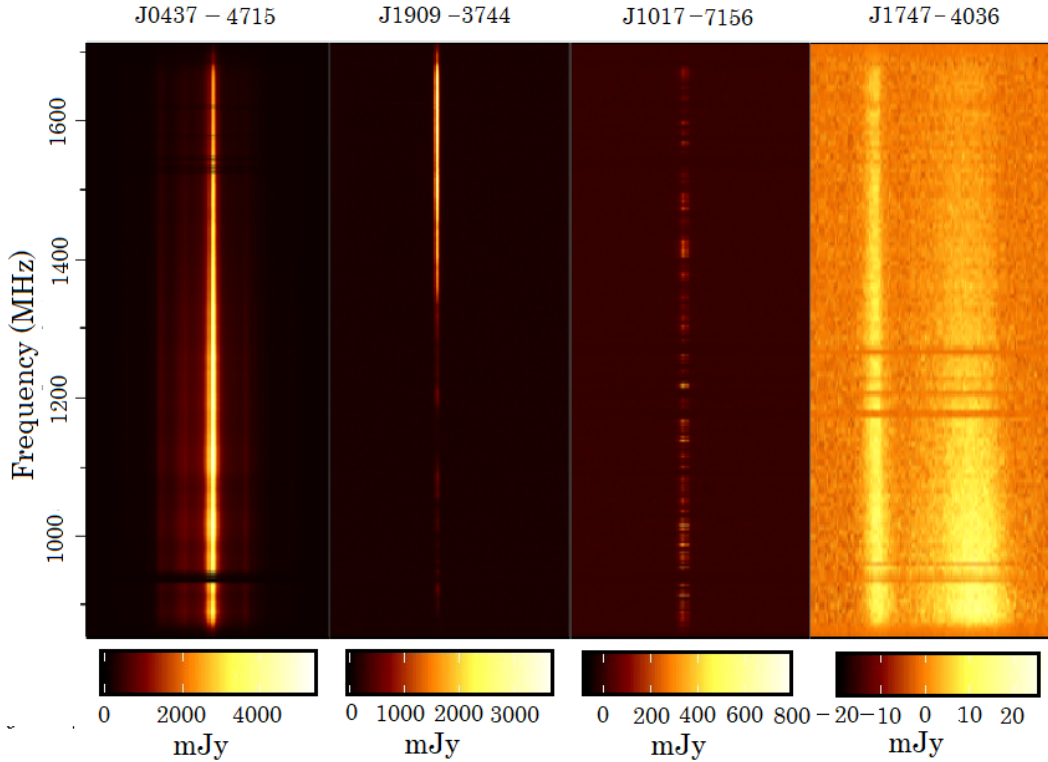


**Figure 1.** The observing frequency versus pulse phase plot of four pulsars at different DMs that experience very different regimes of interstellar scintillation. The horizontal bands present in some of the plots are due to RFI excision such as that near 950 MHz. PSR J0437–4715 (DM  $\sim 2.64 \text{ pc cm}^{-3}$ ) is close to us and exhibits broad band scintillation in the 20 cm band with the flux density never dropping to zero in any part of our observing band. PSR J1909–3744 (DM  $\sim 10.39 \text{ pc cm}^{-3}$ ) often exhibits a sole or a few intense scintillation bands whilst PSR J1017–7156 (DM  $\sim 94.22 \text{ pc cm}^{-3}$ ) often exhibits many bright but narrow scintillation bands across the band. Finally PSR J1747–4036 (DM  $\sim 152.94 \text{ pc cm}^{-3}$ ) has so many scintillation bands that they are unresolved at our observing frequencies.

ratio of their mean flux densities to ours was 0.84 with a standard deviation of 0.19. Clearly, our flux densities are comparable to those of other authors, but may have a bias if the supplied system equivalent flux density from SARAO is in error, or our assumptions about RFI cleaning are invalid. From our comparisons above we suspect that any systematic bias is at most 20%.

### 3.2 Spectral Indices

The radio spectra of pulsars as a function of frequency are often well modelled as a power law

$$S = S_0 \left( \frac{\nu}{\nu_0} \right)^\alpha, \quad (3)$$

where  $S_0$  is the flux density at the reference frequency  $\nu_0$  and  $\alpha$  is the spectral index. In our study, the spectral index for each pulsar was calculated using the mean flux density values at each frequency sub-band and fitting a simple power law via a least-squares method.

The last two columns in Table 1 list the spectral index and its error calculated using the mean flux densities in the 8 observing frequency sub-bands and a least squares power law fit and Figure 3 shows spectral index fit for 3 MSPs in our sample. All of the MSPs in our sample have negative spectral indices ranging from  $-0.9(3)$  for PSR J0636–3044 based on 56 epochs to  $-3.65(10)$  for PSR J1513–2550 which has 37 observations. The overall sample has a mean spectral index of  $-1.86(6)$ . This result is consistent with the findings from Toscano et al. (1998) who found a mean value of  $-1.8$ .

For the 21 MSPs in common between our sample and Dai et al. (2015), we find a mean spectral index value of  $-1.89(13)$  whereas they find  $-1.71(8)$ . Since their lower frequency band extends down to  $\sim 700$  MHz, this may be due to a slight flattening of the spectra at lower frequencies as is clearly exhibited by PSRs J1600–3053 and J1713+0747 in their sample. The biggest discrepancy between the spectral indices of our data sets was exhibited by PSR J2129–5721 where we measure a spectral index of  $-3.4(3)$  as compared to their much flatter  $-2.12(7)$ . This pulsar has a modulation index of 1.2 at 1429 MHz and hence the mean flux density can vary substantially. From the spectral index fit plot given in their paper for this pulsar, it is also evident that their observations show a large step-change flux density deviation from a linear trend at 3 GHz, probably also due to scintillation. We are therefore not unduly concerned by our slightly steeper spectra.

To determine how well the power law describes our pulsar spectra, we performed a chi-squared test. For most of the pulsars, the reduced  $\chi^2$  value was near unity with only two notable exceptions. PSR J1804–2858 and PSR J1756–2251 both deviated quite strongly from the single power law fit. In the case of PSR J1756–2251 the spectrum appears curved, with evidence of mild flattening at lower frequencies. PSR J1804–2858 on the other hand has the highest DM of all the pulsars in our sample with DM =  $232.5 \text{ pc cm}^{-3}$ , and shows evidence of a scattering tail that spans the entire pulse period in the lowest frequency channels. This negates our assumption in Eqn 2 that there exists a baseline that contains none of the pulsar’s flux density. At low frequencies some of the pulsar’s flux density is thus absorbed

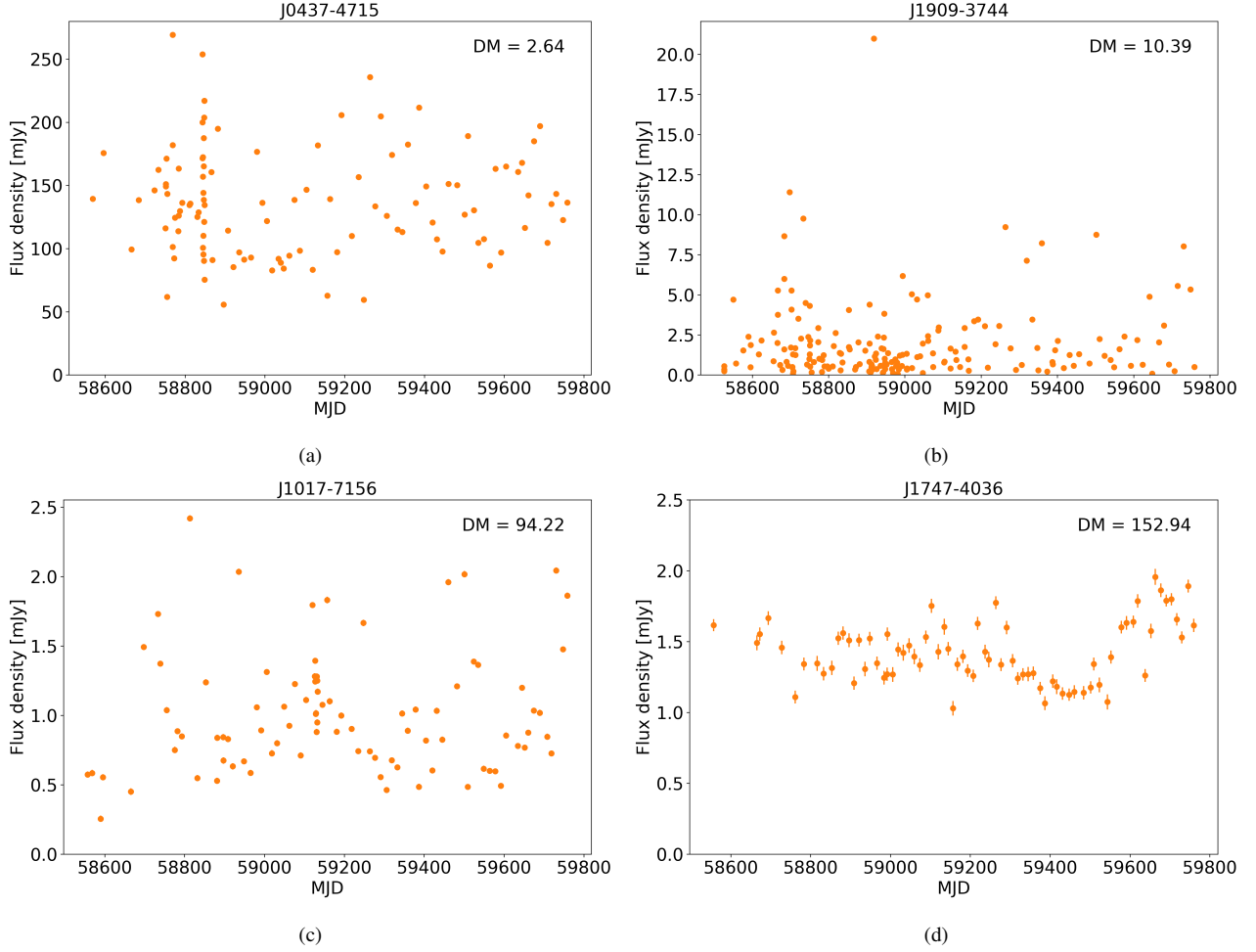


**Figure 2.** Mean flux densities as a function of time for (a) PSR J0437–4715 (b) PSR J1909–3744 (c) PSR J1017–7156 (d) PSR J1747–4036 for a 97 MHz band at a centre frequency of 1429 MHz. Their modulation indices are (a) 0.3 (b) 1.28 (c) 0.43 and (d) 0.15. The error bars in the first three panels are too small to be distinguishable from the data points. The labels show their respective DMs in  $\text{pc cm}^{-3}$ . The apparent vertical stripes in panels (a) and (c) have arisen due to frequent observations of some pulsars as part of non-PTA observing campaigns aimed at studying orbital phase-dependent scintillation and Shapiro delays.

into the baseline leading to an apparent spectral turnover where none might actually exist. For the majority of our pulsars however, there is no evidence for an appreciable spectral turnover over our frequency range. For the population as a whole we investigated whether the average residuals from the power law fit showed any structure as a function of frequency by determining the ratio of the mean flux density to the power law fit in each channel, and then averaging these over the entire population. We found that the mean deviation from the average power law was at most 3% with the lowest frequency bins 1.5% lower, the central bins a few percent higher, and the highest bin lower by 2% suggesting the population as a whole might experience a very mild spectral turnover at the frequencies observed.

### 3.3 Flux density Modulation Indices

To quantify the variability of flux densities of pulsars, a useful parameter is the modulation index

$$m = \frac{\sigma_S}{S_{\text{mean}}}, \quad (4)$$

where  $\sigma_S$  is the standard deviation of the flux densities and  $S_{\text{mean}}$  is the mean flux density in an observing frequency sub-band. Inspection of Table 1 reveals that the modulation indices of the pulsars depend

strongly upon the DM of the pulsar. Higher DM pulsars have a lower modulation index value in comparison to low DM pulsars in general. From Table 1 we find that our largest modulation index was 2.0(4) for the  $\text{DM} = 10.39 \text{ pc cm}^{-3}$  pulsar J1909–3744 at a centre frequency of 1625 MHz based upon 192 observations, while the lowest modulation index of 0.08(1) was for the  $\text{DM} = 114.54 \text{ pc cm}^{-3}$  pulsar J1843–1448 at a centre frequency of 944 MHz based upon 38 observations. There is also a tendency for intermediate DM pulsars to exhibit higher modulation indices at higher frequencies. At 944 MHz, the mean modulation index of the sample is 0.56 and median is 0.40, with a standard deviation of the population 0.39. As we go to higher centre frequencies, at 1429 MHz, the mean, median and standard deviation of modulation index is 0.63, 0.50 and 0.41 respectively. At a centre frequency of 1625 MHz, the mean, median and standard deviation shifts to 0.68, 0.60, and 0.44 respectively. At higher radio frequencies, the differential path lengths of scattered waves are shorter, which results in larger decorrelation scales with frequency and time, and greater modulation of the flux densities.

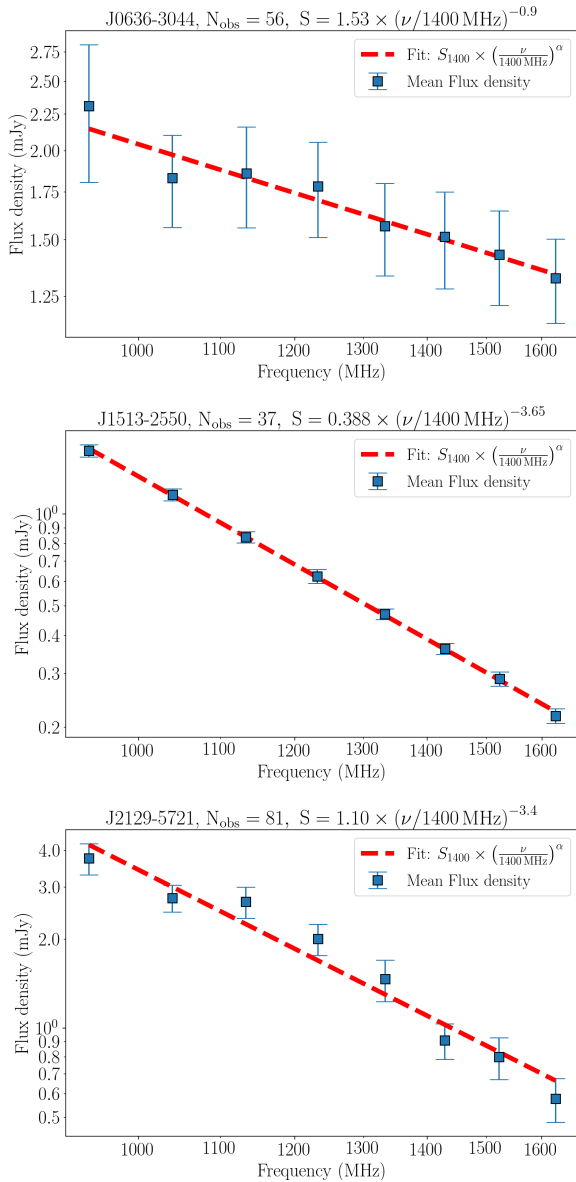


**Figure 3.** Spectra of PSR J0636–3044 (the flattest in our sample) and PSR J1513–2550 (steepest) and J2129–5721, demonstrating the range of pulsar flux density spectra from our sample.

### 3.4 Flux Density Structure Functions

The pulsar flux densities vary on a large range of timescales. A common way to characterise such changes as a function of time is via the use of a temporal structure function. In this way, we can evaluate relative changes on timescales of weeks to years. The flux densities of four pulsars at different DMs are plotted in Figure 2 that illustrate how different pulsar flux densities change with time. Depending on the DM of the pulsar, the flux density either changes independently between observations as shown for pulsars J0437–4715, J1909–3744 and J1017–7156 or more slowly for J1747–4036. We attribute the slow changes in flux density for J1747–4036 are caused by refractive scintillation. To quantify the effects of refractive scintillation on pulsar flux densities, the structure function of the time series of each pulsar was calculated. The structure function formula used here follows the definition by Kumamoto et al. (2021) and gives a mea-

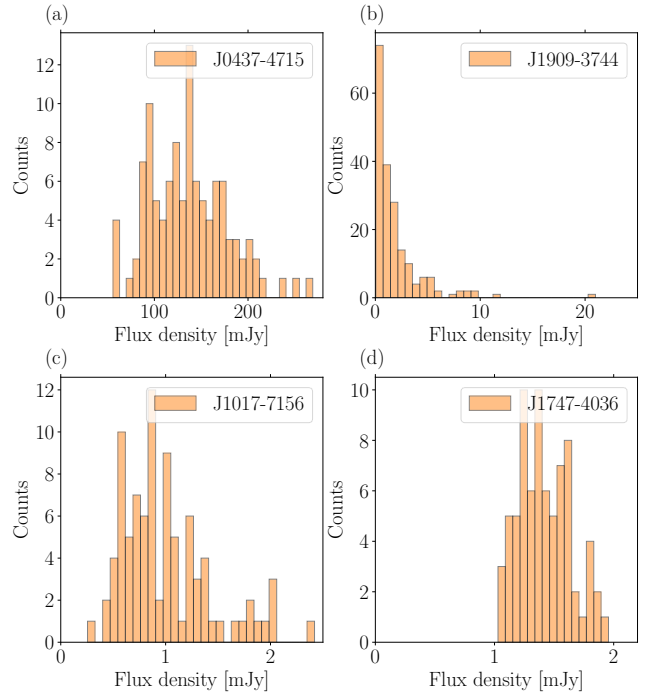


**Figure 4.** Flux density histograms of four pulsars at a centre frequency of 1429 MHz. PSR J0437–4715 with DM  $2.64 \text{ pc cm}^{-3}$ , PSR J1909–3744 with DM  $10.39 \text{ pc cm}^{-3}$ , PSR J1017–7156 with DM  $94.21 \text{ pc cm}^{-3}$  and PSR J1747–4036 with DM  $153 \text{ pc cm}^{-3}$ . As the DM changes we see evolution from a Gaussian-like flux density distribution for J0437–4715 with a small exponential tail, to an almost pure exponential for J1909–3744, back to a Gaussian for J1017–7156 that becomes even more centrally condensed for the high DM pulsar J1747–4036.

sure of the relative change as a function of time. Small values ( $\ll 1$ ) indicate low fractional changes, whereas high values point to large variations. In our study the structure function was calculated in bins of lag starting from 10 days to around 1200 days since our total data span is at most  $\sim 3$  years.

The structure function for a time lag of  $\tau$  is given by

$$D(\tau) = \frac{1}{\bar{S}^2 N_p} \left\{ \sum_{ij}^{N_p} (S_i - S_j)^2 + \sum_{ij}^{N_p} (e_i^2 + e_j^2) + 2 \sum_{ij}^{N_p} (e_i - e_j)(S_i - S_j) - 2 \sum_{ij}^{N_p} e_i e_j \right\}, \quad (5)$$

where  $\bar{S}$  is the average flux density,  $S_i$  is the individual flux densities at each epoch,  $N_p$  is the number of pairs of flux density points that are separated by this lag and  $e_i$  is the uncertainty in measurement of the flux density values. The error in the calculations of the structure functions can be estimated following the derivation in appendix A of You et al. (2007) as

$$\sigma_D^2(\tau) = \frac{1}{N_p^2} \left\{ \sum_i N_i^2 e_i^4 + 4 \sum_i \sum_j e_i^2 (S_i - S_j)^2 + 4 \sum_{ij} e_i^2 e_j^2 \right\},$$

where  $N_i$  is the number of times a flux density value is used to calculate the structure function at a particular lag.

Structure functions are widely used to study time series and scintillation effects are usually unbiased by irregularly sampled data and



**Table 2.** Table showing the measured refractive scintillation timescale and the slope of structure function of 7 pulsars in our sample of MSPs.

NAME	$\tau_r$ (days)	Slope
J0900–3144	$52^{+20}_{-17}$	$0.53^{+0.21}_{-0.20}$
J0955–6150	$21^{+16}_{-8}$	$0.21^{+0.08}_{-0.07}$
J1431–5740	$37^{+13}_{-10}$	$0.89^{+0.89}_{-0.38}$
J1705–1903	$16^{+6}_{-2}$	$1.14^{+2.06}_{-0.69}$
J1747–4036	$31^{+23}_{-9}$	$0.29^{+0.09}_{-0.08}$
J1756–2251	$163^{+80}_{-41}$	$0.91^{+0.75}_{-0.35}$
J1802–2124	$54^{+8}_{-6}$	$0.84^{+0.16}_{-0.16}$

hence ideal for studying the refractive scintillation in temporal flux density observations. The shape of the function can also be used to estimate the refractive scintillation timescale. These parameters derived from the structure functions inform us about the scattering material or inhomogeneities along the line of sight to the pulsars.

A typical structure function has three distinct regions. At very small lags, the structure function is flat and sensitive to calibration noise, radiometer noise, diffractive noise and pulse to pulse variations introduced due to intrinsic variability of pulsars. This is also known as the “noise” regime. We do not probe this region in our study. At medium lags ( $>$  days), the structure function has an increasing slope and can be modelled using a simple power law on a log-log scale. The log-log slope is usually less than 1 as shown by [Stinebring & Condon \(1990\)](#) and [Kumamoto et al. \(2021\)](#). At large lags in excess of the refractive timescale, the structure function saturates and hence flattens. The lag at which the structure function reaches half of its saturation value is often defined as the refractive scintillation timescale ([Stinebring et al. 2000](#)).

Table 3 shows the structure function values of all the 89 MSPs in our sample at lags of 2 weeks, 1 month, 1 year and 3 years with errors associated with them in brackets. The structure functions shows the complex nature of the temporal variations of the MSPs but can be used to help plan observations, especially if recent observations of the pulsar exist and it has a long refractive timescale. The extremely low values of the 2-week structure function for some pulsars (e.g. J1643–1224 with 0.008(5)) give us great confidence in the stability of the MeerKAT phasing and calibration, and also the validity of our flux density calibration procedure at least on a relative scale.

There are a few different classes of structure functions. Some pulsars show linear increase in the structure function before reaching saturation. Other - mainly low DM pulsars - show no temporal evolution and are essentially constant and cannot have their refractive timescales estimated. Some pulsars only have the increasing slope region and insufficient time spans to reveal the flattened region. In order to estimate the refractive scintillation timescale for our MSPs, we plotted the structure function as function of time lags using the equations described in [Haverkorn et al. \(2004\)](#) using the publicly available structure function package from Thomson<sup>1</sup>. Figure 5 shows the computed structure function of 7 MSPs at a central frequency of 1429 MHz. Only seven of our pulsars exhibited linear trends in their log-log plots and clear saturation. The refractive scintillation timescale for the 7 pulsars for which we could measure it are presented in Table 2.

Seven MSPs in our sample are in common with the study of

[Wang et al. \(2023\)](#), so we compared our results. Only two of the MSPs had refractive timescales ( $\tau_r$ ) measured in both studies but they are both in good agreement. For PSR J0900–3144 we measured  $\tau_r = 52^{+20}_{-17}$  d whereas they found  $\tau_r = 51.7$  d, while for J1802–2124, we had  $\tau_r = 54^{+8}_{-6}$  d and they had  $\tau_r = 50.5$  d.

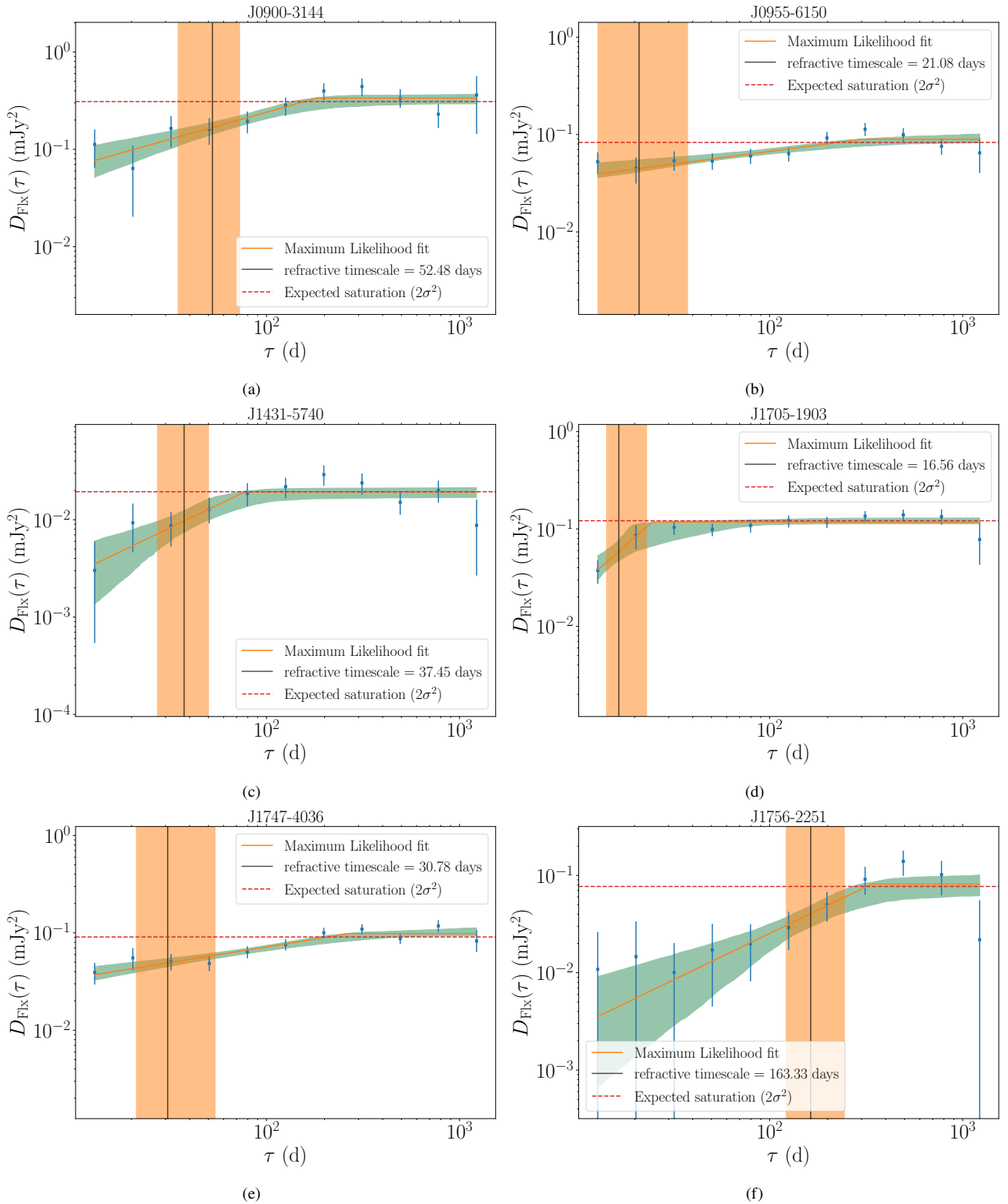
The slope of the structure function in the log-log plot provides information about the power spectrum of the inhomogeneities in the ISM. Most of the pulsars have a slope  $<$  1 which is consistent with the studies of [Kumamoto et al. \(2021\)](#). The slope of the structure function is related to the IISM distribution along the line of sight. As suggested by [Romani et al. \(1986\)](#) a slope of  $\sim 2$  would be indicative of a Kolmogorov spectrum with a thin screen model, but in our sample, only the intermediate-DM MSP J1705–1903 had a slope of 1.14, and the other 6 had slopes of  $<$  1. These results are consistent with previous studies of [Stinebring et al. \(2000\)](#) and [Kumamoto et al. \(2021\)](#) suggesting an extended scattering media along the line of sight. The highest slope of 1.4 is seen by the lowest DM pulsar J1705–1903 out of the 7 MSPs, suggesting a thin scattering screen for lower DM pulsars. This MSP is unique in our sample, as it is a black widow ([Morello et al. 2019](#)), and known to be prone to interactions with material in the near vicinity of the pulsar that cause depolarisation and absorption. Some of the flux density variations in this pulsar are thus localized to the source.

## 4 DISCUSSION

An inspection of Table 1 reveals that the average modulation indices vary as a function of DM and in Figure 6 we plot the means and standard deviations in 9 DM bins for our 89 MSPs. At 944 MHz the mean modulation index starts near unity and drops off to about a third of that value by a DM of  $50 \text{ pc cm}^{-3}$  before settling at 0.2 at the highest DMs. At 1625 MHz the peak is shifted to slightly higher DMs, starting at 0.8, peaking at 1.2 by a DM of  $\sim 25 \text{ pc cm}^{-3}$  before dropping to about 0.45 by a DM of  $60 \text{ pc cm}^{-3}$  and finally reaching a value of near 0.2 at the highest DMs. This behaviour is similar to that seen by other authors. Both [Stinebring et al. \(2000\)](#) and [Jankowski et al. \(2018\)](#) showed that the modulation index of ‘normal’ pulsars decrease with an increase in DM and are consistent with our results for the MSPs as shown in Figure 6. Since we are probing the effects of IISM, not the intrinsic pulsar emission, we would expect both ‘normal’ pulsars and MSPs to have consistent modulation index variation with DM. The mean modulation index is always lower at the low frequency than the higher frequency equivalent except for the lowest DM bins where the flux density variations are higher. For bins with very large DMs, the mean modulation index is similar for all the observing frequencies. As we go towards higher frequencies, the scattering is weaker hence the modulation index is higher at higher frequencies in comparison to its lower frequency counterpart. [Wang et al. \(2023\)](#) have shown that there exists a negative correlation between modulation index and the assumed distance of pulsars, but as distance is a proxy for DM, this is consistent with our findings.

We identify three broad regions in Figure 6. The first bin is populated by the very low DM pulsars which exhibit a wide range of modulation indices. The mean modulation indices peak around a DM of  $20 \text{ pc cm}^{-3}$  before reducing to more stable values near 0.2 at high DMs in excess of  $100 \text{ pc cm}^{-3}$ . For all of the pulsars with a DM greater than  $100 \text{ pc cm}^{-3}$ , the mean modulation index is less than  $\sim 0.4$  which is consistent with the results from [Wang et al. \(2023\)](#) who have done similar analysis on a sample of both slow and millisecond pulsars. Our study has therefore shown that like the slow pulsars, MSPs have low flux density modulation indices at high DMs and are

<sup>1</sup> <https://github.com/AlecThomson/structurefunction>



therefore almost certain to have stable intrinsic radio luminosities (in the absence of intrinsic properties such as eclipses). Scintillation theory (e.g. Scheuer 1968; Cordes et al. 1986; Rickett 2001) predicts different scattering regimes for pulsars that lead to different behaviours. The closest pulsars (low DMs) are close to the regime of weak scintillation, where the difference in the path lengths travelled by different rays are less than 1 radian in phase and there are only

mild changes in the observed mean fluxes. At 20 cm wavelengths such a pulsar is PSR J0437-4715 with a  $\text{DM} = 2.64 \text{ pc cm}^{-3}$ . Its time series is shown in Figure 2(a) and a histogram of its flux densities in Figure 4(a). In a single observation, the pulsar always exhibits a single continuous mildly modulated scintle spanning the whole spectrum as shown in Figure 1(a). Here, the scintillation bandwidth can be much greater than our full observing frequency band and

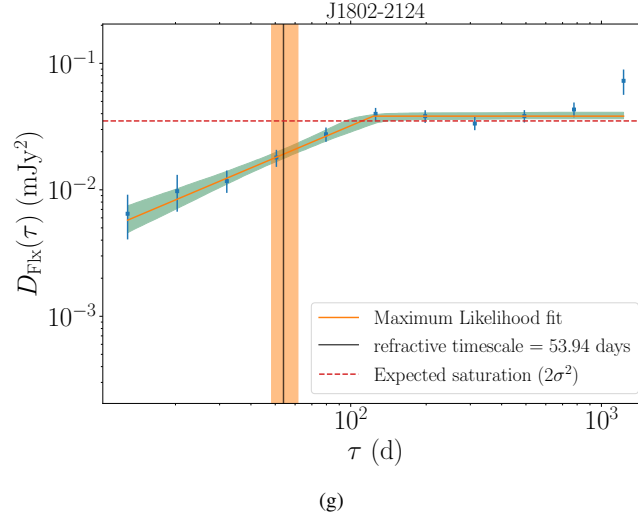


**Figure 5.** Structure function as a function of time lag for (a) PSR J0900–3144 (DM = 75.7 pc cm<sup>-3</sup>) (b) PSR J0955–6150 (DM = 160.9 pc cm<sup>-3</sup>) (c) PSR J1431–5740 (DM = 131.4 pc cm<sup>-3</sup>) (d) PSR J1705–1903 (DM = 57.5 pc cm<sup>-3</sup>) (e) PSR J1747–4036 (DM = 152.9 pc cm<sup>-3</sup>) (f) PSR J1756–2251 (DM = 121.2 pc cm<sup>-3</sup>) (g) PSR J1802–2124 (DM = 149.6 pc cm<sup>-3</sup>) for a 97 MHz band at a centre frequency of 1429 MHz. The shaded orange and green regions show the error associated with the measurement of the refractive timescale and the maximum likelihood fit for the structure function respectively. The red dotted line shows the expected saturation level for a random process with variance  $\sigma^2$  for time lags much larger than the associated timescale.

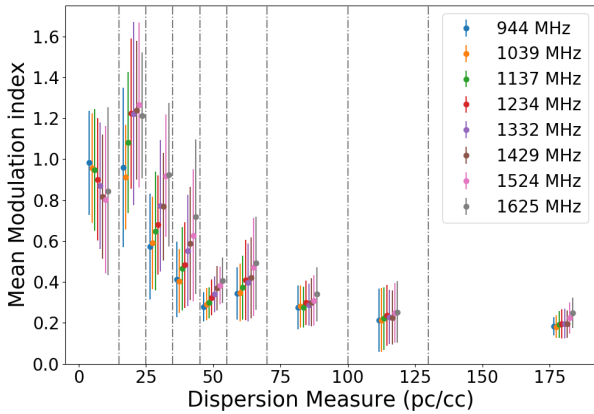


**Figure 6.** Variation of modulation index with DM of 89 MSPs at 8 different centre observing frequencies. The mean value of the modulation index is calculated for every pulsar in each bin where the DM boundaries are 0, 15, 25, 35, 45, 55, 70, 100, 130 and 240 pc cm<sup>-3</sup> shown as dotted vertical lines. The mean modulation index values for the different frequencies are shown with a small offset from the true bin centre to show the error bars that represent the standard deviations more clearly.

hence, although its flux density varies, its modulation index is quite modest. Curiously, despite its very similar DM of 3.14 pc cm<sup>-3</sup> and distance of  $\sim 400$  pc, PSR J1744–1134 has a large modulation index of 1.0(2) at 1429 MHz. Clearly on 150–400 pc scales particularly at low galactic latitudes the Galaxy can have very different diffractive properties.

Higher DM pulsars like PSR J1909–3744 (DM = 10.39 pc cm<sup>-3</sup>) are in the strong scintillation regime for our observing frequencies. In these cases, the scintillation bandwidth is less than our observed spectral range often causing one or more bright scintles to appear as shown in Figure 1(b). In this strong scintillation regime, the effects are extreme, causing amplified flux intensities but also sometimes nulls. This leads to the exponential distribution that is shown in Figure 4(b) for PSR J1909–3744. The time series plot for this pulsar

in Figure 2(b) shows seemingly random pulsar flux densities causing its high observed modulation index of up to 2.0(4) at 1625 MHz.

As the DM increases further e.g. for PSR J1017–7156 with DM = 94.22 pc cm<sup>-3</sup>, the scintillation bandwidth is reduced further and a multitude of small-bandwidth scintles appear throughout the frequency spectrum (Figure 1(c)). The averaging of flux densities in our bands results in more stable fluxes and a lower modulation index. Because of the central limit theorem the flux density histograms tend towards a Gaussian distribution but are still slightly skewed as seen in Figure 4(c).

For very high DM pulsars like PSR J1747–4036, the scintillation bandwidth gets even smaller and small bandwidth scintles become so numerous that they are almost unresolved the flux density becomes almost continuous across the observing bandwidth (see Figure 1(d)). Here slow variations in the flux densities arise due to the focussing and defocussing of the radio waves through the IISM via the process of refractive scintillation. The flux density histogram for this pulsar in Figure 4(d) displays a narrower fractional width Gaussian distribution. The slow variations of flux densities can be explored to estimate the refractive scintillation timescales which are described in detail in subsection 3.4. The modulation index of PSR J1747–4036 is 0.15(1) at a centre frequency of 1429 MHz which is much smaller than that the 1.3(2) seen for PSR J1909–3744. The value of the structure function at a time lag of 2 weeks is very small and only 0.020(3). Our results are consistent with [Stinebring et al. \(2000\)](#) and [Wang et al. \(2023\)](#) who showed that the high DM pulsars have low modulation indices and are probably of near constant intrinsic luminosity. Our high DM pulsar low modulation indices and structure function values also give us confidence that our flux density calibration methods are reliable.

It is interesting to examine how the pulsar modulation indices vary as a function of Galactic location. Figure 7 shows the Aitoff-Hammer projection of all 89 MSPs in our sample. MSPs along the Galactic plane usually have low modulation indices because of their higher DMs in comparison to those in the off plane region. This makes sense as there is more clumpy ionised plasma in the Galactic plane containing the Galaxy’s spiral arms in comparison to the off plane

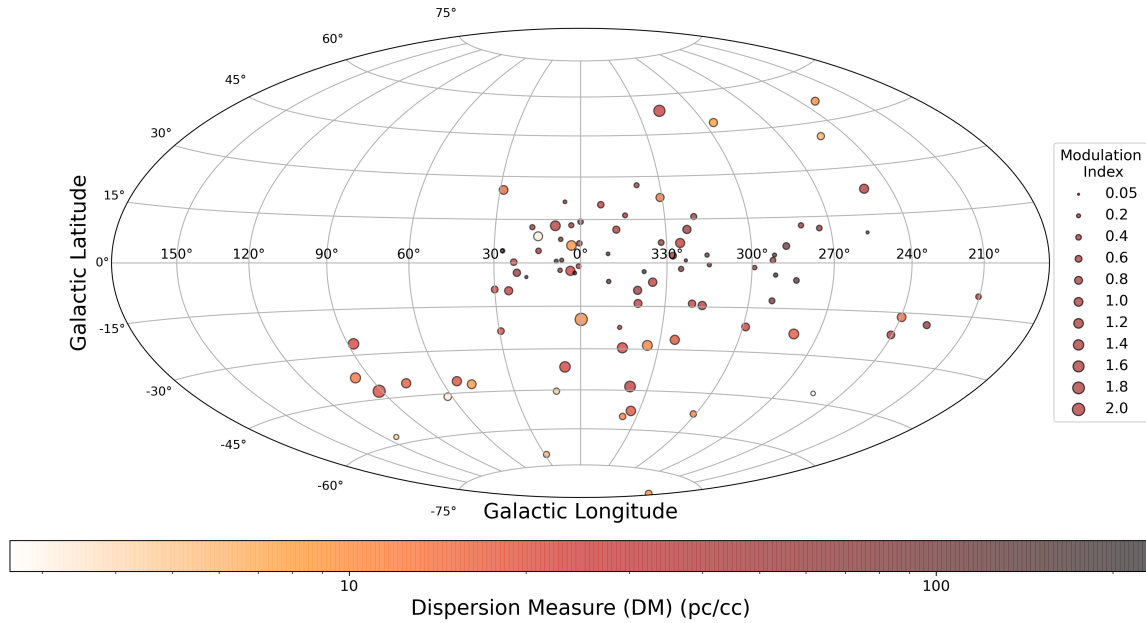


**Figure 7.** Aitoff-Hammer projection of the 89 MSPs in our sample. The area of the dots is proportional to their 1429 MHz modulation index and their DMs are represented by different colours as per the legend. The MSPs between Galactic latitudes of  $15^\circ < |b| < 45^\circ$  show high variability in their flux densities due to the nature of the scattering screens along their lines of sight.

region where there is much less material and scattering along the line of sight to the pulsars. It is very rare that  $DM \sin b$ , where  $b$  is the Galactic latitude, exceeds  $25 \text{ pc cm}^{-3}$  whereas pulsars in the Galactic plane often have DMs greater than  $100 \text{ pc cm}^{-3}$  and sometimes over  $1000 \text{ pc cm}^{-3}$ . A higher modulation index value is seen between Galactic latitudes  $15^\circ < |b| < 45^\circ$  and thus represents the most highly scintillating part of the Galactic sky at these wavelengths. There are a few pulsars that lie in the Galactic plane but still exhibit high variability despite having a high DM, presumably due to some combination of their kinematics and makeup on the ISM along their line of sight. For instance PSR J1103–5403 has a modulation index of 0.54(8) even though its DM is  $103.91 \text{ pc cm}^{-3}$ , but PSR J1843–1448 has only a slightly higher DM of  $114.54 \text{ pc cm}^{-3}$  (both are located at similar angular displacement from the Galactic plane) but a modulation index of only 0.11(1) at the same frequency. PSR J1103–5403 is known to be mode-changing (Nathan et al. 2023), which is clearly seen when we explore the timing residuals of this pulsar and the residuals can be grouped into two distinct emission ‘modes’. To explore if the relatively high modulation index of this pulsar is due to the different modes, we calculated the flux densities of the observations in each of the two modes and found that the median flux density of the “upper” mode was 1.8 times that of the “lower” mode (where the timing residuals are higher in the “upper” mode than the “lower”). The modulation indices of the two modes were 0.55(9) and 0.44(9) for the upper and lower modes respectively, whereas the modulation index of all of the observations was 0.60(8) which demonstrates the effect of emission modes on the results.

#### 4.1 Implications for PTA observing strategy

Our structure functions, modulation indices and ratios of peak to median fluxes for our 89 MSPs allow us to explore whether dynamic scheduling, in which we can dwell longer on a source in a favourable scintillation state can improve a PTA’s timing precision. The radiometer signal-to-noise’s dependence upon flux (linear) and

integration time ( $\propto t^{1/2}$ ) (Eqn 2) provides the motivation. Pulsars in a high flux state many times their median are thus far more valuable. Unfortunately, many pulsars are jitter-limited and do not necessarily benefit from increased SNR (e.g. Osłowski et al. 2011; Shannon et al. 2014; Parthasarathy et al. 2021) but nevertheless we can compute what benefits we might see for pulsars with very low amounts of jitter. Following Siemens et al. (2013), the signal to noise ratio  $snr$  of detection of gravitational wave background (GWB) in PTAs in “weak signal limit” is given by

$$snr \propto Mc \frac{A^2}{\sigma^2} T^\beta \quad (6)$$

where  $M$  is the number of pulsars in the PTA,  $c$  and  $T$  are the cadence and timespan of observations,  $A$  and  $\beta$  are the amplitude and spectral index of the GWB and  $\sigma$  is the error in the times of arrivals (ToAs) of the pulsars. We can estimate the effect of different observation strategies on the detectability of GWB by a PTA using Eqn 6. We considered a strategy where any time observers find a flux density in the top quartile for that pulsar they dwell on it for 4 times as long, at the expense of three other pulsars that are in a low flux density state. For each of the 89 pulsars in the MPTA we therefore computed the ratio of the sum of 4 times the signal-to-noise ratios squared of the top quartile of observations, and compared them to that of all the observations across the entire MeerKAT observing band. This number, between 1-4, gives the improvement in the gravitational wave detection signal-to-noise ratio and is plotted in Figure 8 as a function of the modulation index. The choice of the top quartile is somewhat arbitrary, but if the objective is to detect low-frequency gravitational waves it is probably necessary to observe at least 6 times per year, and this is about 1/4 of the current cadence being achieved for the MPTA. From our Figure we can see that even pulsars with a modest modulation index of 0.2 achieve a 50% improvement in detection signal-to-noise and those near unity are closer to a factor of 3.25.

MeerKAT will eventually become part of the 196-dish SKA-Mid. One could imagine a 16 element sub-array quickly performing a

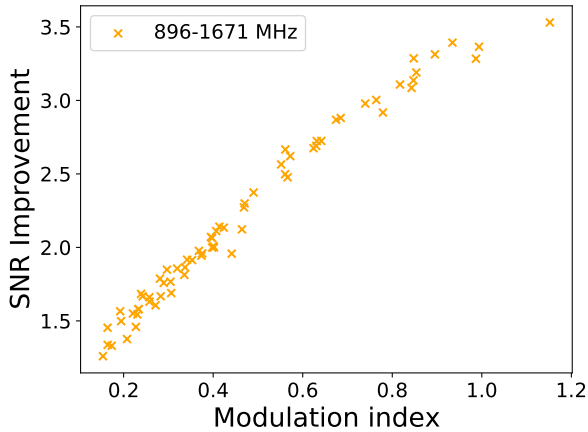


**Figure 8.** Improvement in the SNR of the detected GWB versus flux density modulation index of the pulsars in our MSP sample with more than 60 observations for the full frequency band.

census of the flux state of the next few pulsars in the schedule and then joining the rest of the antennas to monitor the pulsars in favourable scintillation states (Parthasarathy et al. 2021). According to our current understanding, the GWB is only present at very low (nHz) frequencies, hence a shorter cadence won’t affect the Hellings and Downs cross-correlation curve presence required for the detection of GWs. Another potential penalty that might arise from “scint-hunting” is that a small uncertainty in the arrival time in one sub-band is only of value if the DM can be accurately determined, and this is sometimes compromised when there is insufficient flux across the band to accurately determine the DM. In such cases the uncertainty in the DM dominates the arrival times.

#### 4.2 Implications of the IISM for FRB discovery rates and FRB luminosities

FRBs are transient events in the sky that are of unknown astronomical origin which are highly energetic, on time scales of  $\mu\text{s}$  to tens of milliseconds (e.g. Lorimer et al. 2007; Bailes 2022). Because of their immense distances, FRBs are expected to be point sources and like pulsars the IISM is expected to amplify the flux densities of FRBs, and might affect their observed population at different galactic latitudes (Macquart & Johnston 2015; Kumar et al. 2017). We expect scintillation to more frequently amplify FRBs at high Galactic latitudes than near the plane, as shown in simulations by Petroff et al. (2014). Hence, the inferred luminosities of especially one-off FRBs at high latitudes might be systematically overestimated in FRB surveys.

We studied this using Monte Carlo simulations of synthetic populations of cosmologically distributed FRBs, assuming a flux-limited detection threshold, including scintillation effects due to the IISM. Each FRB was placed in a volume up to a maximum distance well beyond our detection threshold. The FRB luminosity function is known to have a wide energy distribution as described in (e.g. James et al. 2022; Shin et al. 2023). For simplicity we considered a log-normal distribution as the extent of the luminosity function is more important than its shape and assigned each simulated FRB an intrinsic luminosity and calculated the flux density. This flux density was then multiplied by a magnification factor which was drawn from an exponential distribution (similar to that of PSR J1909–3744 - see Figure 4 (b)), to represent FRBs affected by strong scintillation where it

is well approximated by an exponential. If the scintillated flux was greater than our detection threshold we recorded it as a detection, and the luminosity, distance and flux recorded.

We found that in the exponential-distribution scintillation case, the average distance up to which we can detect FRBs is  $\sim 2.35$  times more than in the no-scintillation case. Therefore surveys in directions where scintillation is as high as seen in PSR J1909–3744 could have FRB discovery rates increased by  $\sim 32\%$ . We also found that on average the FRBs in the exponential-scintillation case have their mean luminosities overestimated by a factor of about 2.4. But is this borne out by current FRB surveys? Interestingly, in by far the most prolific FRB survey undertaken by CHIME, Josephy et al. (2021) found no evidence for any dependence between FRB detection and Galactic latitude by performing statistical tests on CHIME FRBs taking into account many selection effects such as telescope sensitivity, dwell time with declination etc. They found that in the CHIME observing frequency band (400–800 MHz), strong scintillation effects, of the type we see in this sample, are not a factor. Our simulations predicted that FRB surveys will be  $\sim 30\%$  more prolific if they survey regions of the Galaxy prone to high degrees of scintillation or at a higher observing frequency and it will be interesting to see if this is borne out by future surveys at frequencies similar to that of the MPTA data such as that of TRAPUM (Stappers & Kramer 2016) and MeerTRAP (Stappers 2016).

## 5 CONCLUSIONS

We presented the flux density variability of 89 MSPs based upon regular observations of the MeerKAT Pulsar Timing Array. Despite the lack of a pulsed cal, we were able to show that our derived flux densities are reliable and suitable for modulation index and structure function analyses. Our study demonstrates that MSPs on the whole have simple power law spectra over the range 856–1712 MHz, with only a very modest tendency for any curvature. We demonstrated that the MSPs all vary in flux density, but this is a strong function of their DMs and indicates that MSPs have intrinsically stable radio luminosities. Our results will help in planning future timing array and Shapiro delay campaigns with both MeerKAT and other existing and future 20 cm band radio telescopes such as the SKA and the Deep Synoptic Array 2000. Pulsars with high DMs and long refractive scintillation timescales can have their flux densities reliably predicted from epoch to epoch. Our variability metrics can also be used to optimise timing array observation strategies. Finally, our simulations predict that 20 cm FRB surveys should have more success at finding distant FRBs at the mid-galactic latitudes where the modulation indices of MSPs peak.

## ACKNOWLEDGEMENTS

The MeerKAT telescope is operated by the South African Radio Astronomy Observatory, which is a facility of the National Research Foundation, an agency of the Department of Science and Innovation. PG acknowledges the support of an SUT post graduate stipend. RMS, MB and DJR acknowledge support through the Australian Research Council (ARC) centre of Excellence grant CE17010004 (OzGrav). RMS acknowledges support through ARC Future Fellowship FT190100155. This work used the OzSTAR national facility at Swinburne University of Technology and the pulsar portal maintained by ADACS at URL: <https://pulsars.org.au> OzSTAR and the pulsar portal

**Table 3.** Measured flux density structure functions of the 89 MSPs in our sample at a central frequency of 1429 MHz at a time lag of 2 weeks, 1 month, 1 year and 3 years.

NAME	DM (pc cm <sup>-3</sup> )	D( $\tau$ ) (2 weeks)	D( $\tau$ ) (1 month)	D( $\tau$ ) (1 year)	D( $\tau$ ) (3 yrs)
J0030+0451	4.33	0.258(7)	0.326(3)	0.292(1)	0.318(2)
J0101-6422	11.92	0.765(4)	0.486(1)	0.5703(9)	0.554(1)
J0125-2327	9.6	0.63(2)	0.80(1)	0.941(4)	0.875(4)
J0437-4715	2.64	0.2(7)	0.2(3)	0.2(2)	0.2(2)
J0610-2100	60.69	0.434(5)	0.690(3)	0.611(1)	0.798(1)
J0613-0200	38.78	0.175(8)	0.381(5)	0.306(2)	0.283(2)
J0614-3329	37.05	1.179(8)	1.329(3)	1.469(2)	1.253(1)
J0636-3044	15.46	1.91(4)	2.86(2)	2.911(9)	2.511(9)
J0711-6830	18.41	2.32(6)	6.44(4)	5.26(2)	5.02(2)
J0900-3144	75.69	0.009(4)	0.011(2)	0.027(1)	0.022(1)
J0931-1902	41.49	1.628(8)	0.929(3)	1.304(2)	2.721(3)
J0955-6150	160.9	0.138(3)	0.129(1)	0.2235(8)	0.2162(8)
J1012-4235	71.65	0.2260(6)	0.2296(3)	0.2452(2)	0.2404(2)
J1017-7156	94.22	0.270(3)	0.299(1)	0.3553(6)	0.3962(7)
J1022+1001	10.25	1.66(4)	1.70(2)	1.578(6)	1.661(7)
J1024-0719	6.49	1.16(2)	0.913(7)	1.116(3)	0.947(3)
J1036-8317	27.09	0.749(4)	1.182(2)	1.576(1)	1.264(1)
J1045-4509	58.11	0.18(1)	0.191(5)	0.233(2)	0.226(2)
J1101-6424	207.36	0.0257(7)	0.0452(4)	0.0603(3)	0.0760(4)
J1103-5403	103.91	0.525(2)	0.554(1)	0.5762(5)	0.6016(5)
J1125-5825	124.82	0.061(3)	0.060(1)	0.0896(9)	0.138(1)
J1125-6014	52.93	0.264(9)	0.249(4)	0.242(2)	0.304(2)
J1216-6410	47.39	0.133(6)	0.136(3)	0.131(1)	0.141(1)
J1231-1411	8.09	1.338(6)	1.600(6)	2.376(6)	1.89(3)
J1327-0755	27.91	2.947(4)	2.290(2)	3.024(1)	2.745(1)
J1421-4409	54.64	0.33(1)	0.400(5)	0.397(2)	0.347(2)
J1431-5740	131.38	0.0213(4)	0.0739(3)	0.1734(2)	0.1195(2)
J1435-6100	113.78	0.0707(4)	0.0684(2)	0.08210(9)	0.08636(9)
J1446-4701	55.83	0.929(3)	0.936(2)	0.8870(7)	0.9578(7)
J1455-3330	13.57	0.749(6)	2.247(4)	2.404(2)	2.475(2)
J1513-2550	46.88	0.074(2)	0.101(1)	0.1288(8)	0.144(1)
J1514-4946	31.01	0.418(2)	0.952(1)	1.3388(7)	1.394(1)
J1525-5545	126.97	0.0111(3)	0.0106(2)	0.0255(1)	0.0515(2)
J1543-5149	50.98	0.46(1)	0.638(5)	0.795(2)	0.549(2)
J1545-4550	68.39	0.344(8)	0.283(3)	0.267(1)	0.305(2)
J1547-5709	95.72	0.170(2)	0.244(1)	0.2127(8)	0.2116(8)
J1600-3053	52.33	0.203(7)	0.185(3)	0.173(1)	0.164(1)
J1603-7202	38.05	1.13(3)	1.43(1)	1.139(5)	1.283(6)
J1614-2230	34.49	0.278(9)	0.402(4)	0.424(2)	0.435(2)
J1628-3205	42.14	0.42(1)	1.26(1)	0.503(5)	0.631(4)
J1629-6902	29.49	0.682(6)	0.933(3)	0.821(1)	0.781(1)
J1643-1224	62.4	0.008(5)	0.013(3)	0.021(2)	0.055(2)
J1652-4838	188.16	0.033(2)	0.047(1)	0.0497(7)	0.0682(7)
J1653-2054	56.52	0.217(4)	0.308(2)	0.328(1)	0.273(1)
J1658-5324	30.83	2.73(2)	2.000(7)	2.273(3)	1.963(4)
J1705-1903	57.51	0.084(2)	0.205(1)	0.2595(6)	0.2819(8)
J1708-3506	146.77	0.013(3)	0.012(2)	0.013(1)	0.033(2)
J1713+0747	15.99	1.07(6)	2.55(4)	2.28(2)	2.66(2)
J1719-1438	36.78	1.747(5)	1.237(2)	1.0497(7)	1.1058(8)
J1721-2457	48.23	0.348(9)	0.331(4)	0.394(2)	0.364(2)
J1730-2304	9.63	0.94(5)	1.75(3)	1.60(1)	1.40(1)
J1731-1847	106.47	0.074(4)	0.112(3)	0.107(2)	0.136(3)
J1732-5049	56.82	1.79(3)	1.97(1)	1.727(5)	1.272(5)
J1737-0811	55.3	0.071(4)	0.121(2)	0.129(1)	0.152(1)
J1744-1134	3.14	2.01(4)	2.01(2)	2.140(8)	1.908(8)
J1747-4036	152.94	0.020(3)	0.024(2)	0.047(1)	0.049(1)
J1751-2857	42.79	0.138(2)	0.1521(9)	0.1599(5)	0.1365(5)
J1756-2251	121.23	0.0095(9)	0.0141(5)	0.0519(4)	0.1154(5)
J1757-5322	30.8	0.389(9)	0.461(4)	0.502(2)	0.485(2)
J1801-1417	57.25	0.199(9)	0.248(4)	0.319(2)	0.284(2)
J1802-2124	149.59	0.0119(6)	0.0253(4)	0.0617(3)	0.0724(3)
J1804-2717	24.67	0.95(3)	3.47(3)	3.08(1)	2.05(2)

NAME	DM (pc cm <sup>-3</sup> )	D( $\tau$ ) (2 weeks)	D( $\tau$ ) (1 month)	D( $\tau$ ) (1 year)	D( $\tau$ ) (3 yrs)
J1804–2858	232.52	0.036(5)	0.025(2)	0.029(2)	0.026(2)
J1811–2405	60.62	0.051(4)	0.078(2)	0.092(1)	0.102(1)
J1825–0319	119.56	0.0389(6)	0.0484(4)	0.0614(3)	0.0801(3)
J1832–0836	28.19	1.12(2)	0.825(7)	1.27(4)	1.7(1)
J1843–1113	59.96	0.467(4)	0.386(1)	0.4160(6)	0.4932(7)
J1843–1448	114.54	0.013(1)	0.0161(9)	0.0223(7)	0.0277(9)
J1902–5105	36.25	0.060(2)	0.077(1)	0.0698(6)	0.0736(6)
J1903–7051	19.66	2.18(1)	2.165(4)	2.410(2)	2.416(2)
J1909–3744	10.39	4.70(1)	3.259(3)	3.279(1)	3.189(1)
J1911–1114	30.97	1.05(2)	1.306(8)	0.996(3)	0.683(4)
J1918–0642	26.59	0.30(1)	0.301(5)	0.307(2)	0.282(2)
J1933–6211	11.51	3.81(2)	3.909(8)	4.324(3)	3.604(3)
J1946–5403	23.73	3.566(4)	5.948(2)	5.2545(9)	4.7866(9)
J2010–1323	22.16	0.422(2)	0.3437(9)	0.4034(4)	0.4727(4)
J2039–3616	23.96	2.427(8)	3.112(4)	3.222(2)	2.995(2)
J2124–3358	4.6	0.80(6)	0.72(2)	0.71(1)	0.58(1)
J2129–5721	31.85	1.79(1)	3.028(6)	3.224(3)	2.991(3)
J2145–0750	9.0	4.7(1)	3.03(5)	2.99(2)	2.81(2)
J2150–0326	20.67	2.340(5)	2.298(2)	1.9272(8)	2.772(1)
J2222–0137	3.28	1.394(7)	0.982(2)	1.120(1)	1.154(1)
J2229+2643	22.73	6.28(2)	8.04(1)	8.124(4)	7.506(5)
J2234+0944	17.83	1.78(3)	3.01(1)	2.754(6)	2.447(6)
J2236–5527	20.09	2.111(5)	2.529(3)	2.352(1)	3.404(2)
J2241–5236	11.41	0.71(1)	0.786(5)	0.692(2)	0.772(2)
J2317+1439	21.9	3.97(1)	3.547(5)	3.513(2)	3.848(2)
J2322+2057	13.38	3.749(7)	2.302(2)	2.186(1)	2.256(1)
J2322–2650	6.15	0.468(2)	0.4854(9)	0.4967(5)	0.5032(5)

are funded by Swinburne University of Technology and the National Collaborative Research Infrastructure Strategy (NCRIS).

## DATA AVAILABILITY

The data set used here will be made available along with the manuscript under the DOI <http://dx.doi.org/10.26185/6487ea315602c>. For each MSP, we have included PSRFITs files of pulsar observations which are fully time and polarization averaged and the frequency channels are averaged into 8 sub-bands. We have provided the mean, median flux densities, standard deviations and modulation indices at 8 different frequency bands for all 89 MSPs in a csv file format. Spectral indices and pulsar parameters such as period, global coordinates and DM are also included in the data set. The data set is also available in the MeerTime pulsar portal [pulsars.org.au](http://pulsars.org.au) which contains all of the MSP observations so far, their raw and cleaned profiles, timing residuals and their dynamic spectra. The data is publicly available after 18 months of embargo.

## REFERENCES

Agazie G., et al., 2023, *ApJ*, **951**, L9  
 Antoniadis J., et al., 2023, *arXiv e-prints*, p. [arXiv:2306.16224](https://arxiv.org/abs/2306.16224)  
 Armstrong J. W., Rickett B. J., Spangler S. R., 1995, *ApJ*, **443**, 209  
 Askew J., Reardon D. J., Shannon R. M., 2023, *MNRAS*, **519**, 5086  
 Backer D. C., 1970a, *Nature*, **228**, 42  
 Backer D. C., 1970b, *Nature*, **228**, 1297  
 Bailes M., 2010, in *Relativity in Fundamental Astronomy: Dynamics, Reference Frames, and Data Analysis*. pp 212–217, [doi:10.1017/S1743921309990421](https://doi.org/10.1017/S1743921309990421)  
 Bailes M., 2022, *Science*, **378**, abj3043  
 Bailes M., et al., 2020, *Publ. Astron. Soc. Australia*, **37**, e028

Boyles J., et al., 2013, *ApJ*, **763**, 80  
 Cole T. W., Hesse H. K., Page C. G., 1970, *Nature*, **225**, 712  
 Cordes J. M., 1986, *ApJ*, **311**, 183  
 Cordes J. M., Downs G. S., 1985, *ApJS*, **59**, 343  
 Cordes J. M., Pidwerbetsky A., Lovelace R. V. E., 1986, *ApJ*, **310**, 737  
 Dai S., et al., 2015, *MNRAS*, **449**, 3223  
 Detweiler S., 1979, *ApJ*, **234**, 1100  
 Geyer M., et al., 2021, *MNRAS*, **505**, 4468  
 Haslam C. G. T., Salter C. J., Stoffel H., Wilson W. E., 1982, *A&AS*, **47**, 1  
 Haverkorn M., Gaensler B. M., McClure-Griffiths N. M., Dickey J. M., Green A. J., 2004, *ApJ*, **609**, 776  
 Hellings R. W., Downs G. S., 1983, *ApJ*, **265**, L39  
 Hewish A., Bell S. J., Pilkington J. D. H., Scott P. F., Collins R. A., 1968, *Nature*, **217**, 709  
 James C. W., Prochaska J. X., Macquart J. P., North-Hickey F. O., Bannister K. W., Dunning A., 2022, *MNRAS*, **509**, 4775  
 Jankowski F., van Straten W., Keane E. F., Bailes M., Barr E. D., Johnston S., Kerr M., 2018, *MNRAS*, **473**, 4436  
 Johnston S., Manchester R. N., Lyne A. G., Bailes M., Kaspi V. M., Qiao G., D’Amico N., 1992, *ApJ*, **387**, L37  
 Josephy A., et al., 2021, *ApJ*, **923**, 2  
 Keane E., et al., 2015, in *Advancing Astrophysics with the Square Kilometre Array (AASKA14)*. p. 40 ([arXiv:1501.00056](https://arxiv.org/abs/1501.00056)), [doi:10.22323/1.215.0040](https://doi.org/10.22323/1.215.0040)  
 Kramer M., Xilouris K. M., Lorimer D. R., Doroshenko O., Jessner A., Wielebinski R., Wolszczan A., Camilo F., 1998, *ApJ*, **501**, 270  
 Kramer M., Lange C., Lorimer D. R., Backer D. C., Xilouris K. M., Jessner A., Wielebinski R., 1999, *ApJ*, **526**, 957  
 Kramer M., Lyne A. G., O’Brien J. T., Jordan C. A., Lorimer D. R., 2006, *Science*, **312**, 549  
 Kramer M., et al., 2021a, *Physical Review X*, **11**, 041050  
 Kramer M., et al., 2021b, *MNRAS*, **504**, 2094  
 Kumamoto H., et al., 2021, *MNRAS*, **501**, 4490  
 Kumar P., Lu W., Bhattacharya M., 2017, *MNRAS*, **468**, 2726  
 Lawson K. D., Mayer C. J., Osborne J. L., Parkinson M. L., 1987, *MNRAS*,

- 225, 307
- Levin L., et al., 2013, *MNRAS*, 434, 1387
- Lorimer D. R., Bailes M., McLaughlin M. A., Narkevic D. J., Crawford F., 2007, *Science*, 318, 777
- Macquart J.-P., Johnston S., 2015, *MNRAS*, 451, 3278
- Manchester R. N., et al., 2001, *MNRAS*, 328, 17
- Manchester R. N., Hobbs G. B., Teoh A., Hobbs M., 2005, *AJ*, 129, 1993
- Miles M. T., Shannon R. M., Bailes M., Reardon D. J., Buchner S., Middleton H., Spiewak R., 2022, *MNRAS*, 510, 5908
- Miles M. T., et al., 2023, *MNRAS*, 519, 3976
- Morello V., et al., 2019, *MNRAS*, 483, 3673
- Nathan R. S., Miles M. T., Ashton G., Lasky P. D., Thrane E., Reardon D. J., Shannon R. M., Cameron A. D., 2023, *arXiv e-prints*, p. [arXiv:2304.02793](https://arxiv.org/abs/2304.02793)
- Ord S. M., van Straten W., Hotan A. W., Bailes M., 2004, *MNRAS*, 352, 804
- Osłowski S., van Straten W., Hobbs G. B., Bailes M., Demorest P., 2011, *MNRAS*, 418, 1258
- Parthasarathy A., et al., 2021, *MNRAS*, 502, 407
- Petroff E., et al., 2014, *ApJ*, 789, L26
- Reardon D. J., et al., 2020, *ApJ*, 904, 104
- Rickett B. J., 1969, *Nature*, 221, 158
- Rickett B., 2001, *Ap&SS*, 278, 5
- Rickett B. J., Coles W. A., Bourgois G., 1984, *A&A*, 134, 390
- Romani R. W., Narayan R., Blandford R., 1986, *MNRAS*, 220, 19
- Scheuer P. A. G., 1968, *Nature*, 218, 920
- Shannon R. M., et al., 2014, *MNRAS*, 443, 1463
- Shin K., et al., 2023, *ApJ*, 944, 105
- Siemens X., Ellis J., Jenet F., Romano J. D., 2013, *Classical and Quantum Gravity*, 30, 224015
- Smits R., Kramer M., Stappers B., Lorimer D. R., Cordes J., Faulkner A., 2009, *A&A*, 493, 1161
- Sobey C., et al., 2021, *MNRAS*, 504, 228
- Spiewak R., et al., 2022, *Publ. Astron. Soc. Australia*, 39, e027
- Stairs I. H., Thorsett S. E., Camilo F., 1999, *ApJS*, 123, 627
- Stappers B., 2016, in *MeerKAT Science: On the Pathway to the SKA*. p. 10, [doi:10.22323/1.277.0010](https://doi.org/10.22323/1.277.0010)
- Stappers B., Kramer M., 2016, in *MeerKAT Science: On the Pathway to the SKA*. p. 9, [doi:10.22323/1.277.0009](https://doi.org/10.22323/1.277.0009)
- Stinebring D. R., Condon J. J., 1990, *ApJ*, 352, 207
- Stinebring D. R., Smirnova T. V., Hankins T. H., Hovis J. S., Kaspi V. M., Kempner J. C., Myers E., Nice D. J., 2000, *ApJ*, 539, 300
- Thornton D., et al., 2013, *Science*, 341, 53
- Thorsett S. E., Chakrabarty D., 1999, *ApJ*, 512, 288
- Toscano M., Bailes M., Manchester R. N., Sandhu J. S., 1998, *ApJ*, 506, 863
- Wang Z., Wang J., Wang N., Dai S., Xie J., 2023, *MNRAS*,
- Xue M., et al., 2017, *Publ. Astron. Soc. Australia*, 34, e070
- You X. P., et al., 2007, *MNRAS*, 378, 493
- Zic A., et al., 2023, *arXiv e-prints*, p. [arXiv:2306.16230](https://arxiv.org/abs/2306.16230)

## APPENDIX A: FLUX CALIBRATION EQUATION DERIVATION

In a folded pulsar observation, if there is negligible radio frequency interference, then the noise  $N'$  in each pulsar phase bin for  $N_{\text{bin}}$  bins, is just

$$N' = \frac{T_{\text{rec}} + T_{\text{sky}}}{G \sqrt{BN_p t / N_{\text{bin}}}} = N \sqrt{N_{\text{bin}}} \quad (\text{A1})$$

In an RFI-free pulsar observation the mean flux density can be computed by integrating the counts of the on-pulse bins and subtracting off the best-fit baseline, then determining the average flux density over the entire pulse period.

The rms of the off-pulse region can be equated to the system noise and sky temperature. The baseline has an uncertainty  $\sigma_b$  determined

from the radiometer equation and the number of off-pulse bins in it which contributes to the uncertainty in the flux density

$$\sigma_b = \frac{N'}{\sqrt{N_{\text{off}}}} = \frac{N'}{\sqrt{N_{\text{bin}} - N_{\text{on}}}} \quad (\text{A2})$$

and similarly the uncertainty in the average height  $h$  of the on-pulse bins has an uncertainty  $\sigma_h$

$$\sigma_h = \frac{N'}{\sqrt{N_{\text{on}}}} \quad (\text{A3})$$

So the area of the on-pulse region  $A$  is just

$$A = (h - b)N_{\text{on}} = S \frac{N_{\text{bin}}}{N_{\text{on}}} N_{\text{on}} = S N_{\text{bin}} \quad (\text{A4})$$

and the signal-to-noise ratio of the on-pulse region is

$$\text{snr} = A / (\sigma_A). \quad (\text{A5})$$

Now the uncertainty in  $A$  is the quadrature sum of the uncertainties in  $h$  and  $b$  multiplied by  $N_{\text{on}}$ . So

$$\sigma_A = N_{\text{on}} \sqrt{(\sigma_b)^2 + (\sigma_h)^2} = N' N_{\text{on}} \sqrt{1/(N_{\text{bin}} - N_{\text{on}}) + 1/(N_{\text{on}})} \quad (\text{A6})$$

$$\sigma_A = N' N_{\text{on}} \sqrt{\frac{N_{\text{bin}}}{(N_{\text{bin}} - N_{\text{on}}) N_{\text{on}}}} = N' \sqrt{N_{\text{bin}}} \sqrt{\frac{N_{\text{on}}}{N_{\text{bin}} - N_{\text{on}}}} \quad (\text{A7})$$

so the  $\text{snr}$  of the on-pulse region is just  $A/\sigma_A$

$$\text{snr} = \frac{S N_{\text{bin}}}{N' \sqrt{N_{\text{bin}}} \sqrt{\frac{N_{\text{on}}}{N_{\text{bin}} - N_{\text{on}}}}} = \frac{S \sqrt{N_{\text{bin}}}}{N'} \sqrt{\frac{N_{\text{bin}} - N_{\text{on}}}{N_{\text{on}}}} \quad (\text{A8})$$

$$\text{snr} = \frac{S}{N} \sqrt{\frac{N_{\text{bin}} - N_{\text{on}}}{N_{\text{on}}}} \quad (\text{A9})$$

so we can rearrange to get

$$S = \text{snr} N \sqrt{\frac{N_{\text{on}}}{N_{\text{bin}} - N_{\text{on}}}} = \text{snr} \frac{T_{\text{rec}} + T_{\text{sky}}}{G \sqrt{BN_p t}} \sqrt{\frac{N_{\text{on}}}{N_{\text{bin}} - N_{\text{on}}}} \quad (\text{A10})$$

where here  $S$  is the mean flux density above the baseline.

This paper has been typeset from a  $\text{\TeX}/\text{\LaTeX}$  file prepared by the author.